THE MOTION OF A CYLINDER NEAR A PLANAR WALL UNDER CONFINEMENT

by
ZEYNEP ÖZALP

Submitted to the Graduate School of Engineering and Natural Sciences
in partial fulfilment of
the requirements for the degree of Master of Science

Sabancı University
August 2025

THE MOTION OF A CYLINDER NEAR A PLANAR WALL UNDER CONFINEMENT

Approved by:

Prof. SERHAT YEŞİLYURT .....
(Thesis Supervisor)

Asst. Prof. TUĞÇE YÜKSEL .....

Prof. İLKER TARI .....

Date of Approval: July 23, 2025

ABSTRACT

THE MOTION OF A CYLINDER NEAR A PLANAR WALL UNDER CONFINEMENT

ZEYNEP ÖZALP

Mechatronics Engineering, M.Sc. Thesis, August 2025

Thesis Supervisor: Prof. Serhat Yeşilyurt

Keywords: low-reynolds swimming, stokes flow, rigid body motion

The motion of a cylinder in a viscous fluid near a planar wall under geometric confinement is central to microrobotics, microfluidics, and other low-Reynolds-number transport applications. A cylinder's trajectory arises from hydrodynamic forces and torques that are strongly modulated by geometry and boundary placement (e.g., gap height, domain aspect ratio, and open versus closed lateral boundaries). Prior work has treated infinite and finite cylinders in unbounded domains and cylinders interacting with walls, including deformable interfaces; however, the role of confinement geometry itself remains underexplored. In this thesis, the motion and hydrodynamic loading of infinite and finite-length cylinders across several confinement scenarios, using 2D/3D creeping-flow simulations, is investigated. The results show that confinement geometry significantly alters the force balance and induces complex motion, including behaviors not observed in unbounded or infinite-cylinder cases. The findings provide insight into the origin and nature of macro-flow-induced translation, offering a refined understanding of finite-body hydrodynamics in constrained environments.

ÖZET

SINIRLI GEOMETRILERDE DUVAR YAKININDA SILINDIRLERIN HAREKETI

ZEYNEP ÖZALP

Mekatronik Mühendisliği, Yüksek Lisans Tezi, Ağustos 2025

Tez Danışmanı: Prof. Dr. Serhat Yeşilyurt

Anahtar Kelimeler: düşük reynolds rejiminde yüzme, stokes akışı, katı cisim hareketi

Düzlemsel bir duvarın yanında ve viskoz bir sıvının içinde bulunan bir silindirin hareketi, mikroakışkanlar, mikrorobotik ve düşük Reynolds sayılı rejimde taşınım gibi çeşitli uygulama alanlarında önem taşımaktadır. Silindirin bulunduğu ortamın sınırları ve geometrisi hem silindirin maruz kaldığı hidrodinamik kuvvetler hem de yörüngesi üzerinde güçlü bir etki göstermektedir. Önceki çalışmalarda duvar yanındaki sonlu ve sonsuz uzunluktaki sınırsız alanlarda hareket eden silindirlerin maruz kaldığı hidrodinamik kuvvetleri ve silindirlerin yumuşak, deforme olabilen duvar yanındaki hareketleri incelenmiştir. Fakat 3 boyutlu ve sınırlandırılmış bir alanda silindirin maruz kaldığı kuvvetler ve yörüngesi yeterince araştırılmamış literatürde bir boşluk olarak kalmıştır. Bu tez literatürdeki boşluğu tamamlayıp farklı şekillerde sınırlandırılmış alanda sonlu ve sonsuz silindirin hareketini ve üzerindeki hidrodinamik kuvvetleri incelemeyi amaçlamaktadır. Yapılan simülasyonların sonucunda, silindirin içinde bulunduğu geometrinin ve sınırlandırma şeklinin kuvvet dengesini önemli bir ölçüde değiştirdiği ve kompleks hareketler sergilediğini ortaya çıkarmıştır. Bulgular, makro akış kaynaklı hareketin kökenine bir ışık tutarak sınırlandırılmış ortamlarda sonlu cisimlerin maruz kaldığı hidrodinamik etkilere dair rafine bir anlayış sunmaktadır.

ACKNOWLEDGMENTS

First and foremost, I would like to extend my sincerest gratitude to my supervisor, Prof. Serhat Yeşilyurt, for always being there for me and putting up with my endless questions at any time of the day, no matter where he is. Working with him was an honor and an immense learning experience for me, as his supervision made me grow in many aspects of life. Additionally, I would like to thank my thesis supervisors, Tuğçe Yüksel, for her invaluable support during my thesis process, and İlker Tarı for his valuable evaluation and feedback for this thesis.

As everyone who has ever gotten a master's knows, support from our friends and family is the most essential thing that keeps you sane in this process. Therefore, I would like to extend my special thanks to İlker Sevgen for being there for me in my direst times, providing both emotional support and assistance in my lab work. I couldn't have done it without him. M. Ali Bayraktar, for staying with me through the endless hours of lab work. Also, Yavuz Toksöz for helping me anytime I asked for it, no matter how minimal it was.

I would also like to extend my thanks to my best friends, Umut, Belin, and Nilsu. Your undying support, patience, and ability to stand my whining about anything and everything were the reasons I was able to get this far in life, and I wish to never part from you. Eren and İrem, thank you for welcoming me into your home and life, and also the dear friends I have made along the way, Işıl, Harun, and Feyza. I want to thank you for our chats, which have been the highlight of most days, and your support in my most stressful times has been my rock.

Finally, I would like to thank my family. Mom and Dad, thanks for not letting me repeat a year and making the sacrifices I am sure you have made, and didn't even let me feel. Your undying support has made the person I am today, and I am proud to be your child. My sister Sude, for being my safe space and being my trustworthy companion through these years we have lived together, and my brother, for all the late-night talks we have had in the yard. I always felt like I could tell you anything, and I hope our relationship never changes. Esma, I am sorry that we haven't spent much time together due to our age difference. I am sure you will be great in life, and I am already proud of you for being the person you are.

To my family
None of this would have been possible without them.

Contents

LIST OF TABLES

LIST OF FIGURES

LIST OF ABBREVIATIONS

LIST OF SYMBOLS

δ_{wall}	Non-dimensional gap height for infinite cylinder theory
h_0	Minimum distance between a planar wall and the cylinder
R	Cylinder radius
$f_{\parallel}$	Non-dimensional force on an infinite cylinder translating parallel to a wall
μ	Dynamic viscosity of the fluid
Ω	Angular velocity of the cylinder (non-dimensional)
U	Translational velocity of the cylinder in the x-direction (non-dimensional)
τ	Torque per unit length on an infinite cylinder
V	Translation perpendicular to the wall
$f_{\perp}$	Non-dimensional force on an infinite cylinder translating perpendicular to a wall
$\hat{\mathbf{F}}$	Dimensional hydrodynamic force vector
$\hat{U}$	Dimensional translational velocity
l	Characteristic length in lubrication theory
L	Length of the finite cylinder (non-dimensional)
$\mathbf{e}_x$	Unit vector in the x-direction
$\hat{V}$	Dimensional velocity component
$\mathbf{e}_z$	Unit vector in the z-direction
$\hat{\mathbf{T}}$	Dimensional hydrodynamic torque vector
$\hat{\Omega}$	Dimensional angular velocity
$\mathbf{e}_y$	Unit vector in the y-direction
F	Non-dimensional hydrodynamic force
T	Non-dimensional hydrodynamic torque
R^{FU}	Resistance coefficient relating force to translational velocity
$R^{F\Omega}$	Resistance coefficient relating force to angular velocity (cross-coupling)
R^{TU}	Resistance coefficient relating torque to translational velocity (cross-coupling)
$R^{T\Omega}$	Resistance coefficient relating torque to angular velocity
D	Cylinder diameter
W_x	Domain width in the x-direction (non-dimensional)

W_y	Domain depth in the y-direction (non-dimensional)
W_z	Domain height in the z-direction (non-dimensional)
d_{wall}	Non-dimensional gap height for finite cylinder theory
f	Rotation frequency
$\tilde{f}$	Dimensional rotation frequency
$\tilde{U}$	Dimensional reference velocity
$\tilde{D}$	Dimensional cylinder diameter
$\mathbf{u}$	Non-dimensional fluid velocity vector
x_0, y_0, z_0	Coordinates of the cylinder's geometric center
W	Velocity component in z-direction
w_x, w_z	Angular velocity components
t	Non-dimensional time
p	Non-dimensional pressure
Re	Reynolds number
$\tilde{\rho}$	Dimensional fluid density
$\tilde{U}_{\text{ref}}$	Dimensional reference velocity
$\tilde{\mu}$	Dimensional dynamic viscosity
$\tilde{U}_\tau$	Dimensional tangential speed at the cylinder surface
$\tilde{\Omega}$	Dimensional angular velocity
$\boldsymbol{\tau}$	Shear stress vector
$\mathbf{n}$	Unit normal vector
S_c	Surface of the cylinder
$\boldsymbol{\sigma}$	Cauchy stress tensor
$\mathbf{n}_x$	Unit normal component in the x-direction
$\sum_{\text{cyl}} \mathbf{F}$	Total hydrodynamic force on the cylinder
$\sum_{\text{side}} \mathbf{F}$	Force on the lateral sides of the cylinder
$\sum_{\text{cap}} \mathbf{F}$	Force on the end caps of the cylinder
$\sum_{\text{nip}} \mathbf{F}$	Force originating from the narrow nip region near the wall
$\sum_{\text{side}} \mathbf{F}^p$	Pressure-driven component of the force on the cylinder sides
$\sum_{\text{side}} \mathbf{F}^{\text{shear}}$	Shear-driven component of the force on the cylinder sides
$\sum_{\text{cap}} \mathbf{F}^{\text{flow}}$	Flow-induced pressure force on the end caps
$\sum_{\text{cap}} \mathbf{F}^{\text{drag}}$	Viscous drag force on the end caps
F_x^{EM}	x-component of electromagnetic force
F_x^{hyd}	x-component of hydrodynamic force
$\mathbf{B}$	Magnetic field vector
$\mathbf{A}$	Actuation matrix mapping coil currents to magnetic field/gradient
$\mathbf{i}$	Vector of coil currents

$\mathbf{c}_x^\top$	Calibration vector for the x-component of electromagnetic force

1. INTRODUCTION

The motion of particles and bodies in viscous flows near boundaries is a fundamental problem in fluid mechanics, with relevance spanning biology, physics, and engineering (Lauga, DiLuzio, Whitesides & Stone, 2006; Pak & Lauga, 2014). At the microscale, fluid motion is governed by the low-Reynolds-number (creeping-flow) regime, where inertial effects are negligible and viscous forces dominate (Stokes, 2009). In this limit, the linearity and reversibility of the Stokes equations provide a powerful theoretical framework, yet the presence of nearby boundaries fundamentally alters the flow field. Boundaries break the spatial symmetry of disturbance flows, increasing hydrodynamic drag, modifying rotation–translation coupling, and, in many cases, producing entirely new modes of motion not seen in unbounded domains (Spagnolie & Lauga, 2012).

When a particle moves close to a wall or within a confined geometry, the disturbance it generates interacts with the boundaries and is reflected back into the flow. These wall-mediated interactions can modify translational and rotational mobilities, generate lift or drift forces, and induce trajectory deviations such as reorientation, circling, or trapping (Czajka, Antosiewicz & Długosz, 2019; Lauga et al., 2006). The magnitude and nature of these effects depend not only on the wall separation, but also on the geometry of the particle and confining boundaries, the imposed flow, and the presence of additional surfaces or interfaces. As a result, near-wall hydrodynamics is not merely a boundary condition to be accounted for; it is often the primary factor determining motion, stability, and transport efficiency in microscale systems (Caldag & Yesilyurt, 2019; Koens & Montenegro-Johnson, 2021; Saintyves, Rallabandi, Jules, Ault, Salez, Schönecker, Stone & Mahadevan, 2020; Spagnolie & Lauga, 2012; Zhu, Lauga & Brandt, 2013).

The impact of these effects is evident across a wide range of scientific and technological contexts. In biological systems, microorganisms such as bacteria, sperm cells, and ciliates routinely navigate in proximity to surfaces, where hydrodynamic coupling to the boundary alters swimming speed, orientation, and stability (Ishimoto & Gaffney, 2013; Lauga

et al., 2006). These mechanisms underlie observed behaviors such as accumulation near walls, circular swimming, and boundary-following trajectories, and they play a role in processes from biofilm formation to reproductive guidance (Spagnolie & Lauga, 2012).

In synthetic systems, particularly magnetic and chemically driven microswimmers, similar wall-induced effects can be exploited for targeted transport, but can also introduce challenges such as unintended drift or trapping (Caldag & Yesilyurt, 2019; Lauga et al., 2006; Zhu et al., 2013). In microelectromechanical systems (MEMS), micron-scale gaps lead to lubrication-dominated regimes where viscous resistance, pressure gradients, and squeeze-film effects govern device performance and wear (Choi, Lee, Choi & Maeng, 2010; Day & Stone, 2000; Sen, Wajerski & Gad-el Hak, 1996; Witelski, 1998). In colloidal suspensions and microfluidic devices, particle–wall interactions control sedimentation, sorting, and trapping, providing passive mechanisms for lab-on-a-chip diagnostics and separation processes (Abel, Stangle, Schilling & Aksay, 1994; Daddi-Moussa-Ider, Nasouri, Vilfan & Golestanian, 2021). Across these domains, the interplay between hydrodynamics, confinement geometry, and particle shape dictates function, efficiency, and reliability (Batchelor, 1970; Koens & Montenegro-Johnson, 2021).

Over the past decades, a rich body of theoretical work has emerged to describe these phenomena, beginning with classical solutions for simple geometries, such as spheres translating or rotating near a single wall, and later extending to slender bodies, fibers, and cylinders (Batchelor, 1970; Cox, 1970; Jeffery & Filon, 1922; Mitchell & Spagnolie, 2015). Analytical approaches, often built on the Lorentz Reciprocal Theorem, method of reflections, and lubrication theory, have provided closed-form solutions for idealised configurations (Crowdy, 2011; Happel & Brenner, 1983; Jeffrey & Onishi, 1981). These models have revealed how geometry, aspect ratio, and wall proximity govern mobility and resistance coefficients, and how coupling between translation and rotation emerges in the presence of broken symmetry (Katz, Blake & Paveri-Fontana, 1975; Koens & Montenegro-Johnson, 2021; Teng et al., 2022). While such theoretical progress has been substantial, much of it assumes simplified conditions such as infinite cylinders, single planar walls, or purely two-dimensional configurations.

In reality, many microscale systems involve finite-length bodies within fully three-dimensional confinement, where multiple boundaries interact hydrodynamically and where flow cannot be reduced to a single-wall problem. In these settings, wall-induced coupling can drive unexpected behaviors, including spontaneous slipping, reverse rotation, or trajectory deflection, whose onset depends sensitively on the confinement ratio, body geometry, and boundary arrangement (Caldag, Demir & Yesilyurt, 2022; Caldag & Yesilyurt, 2019; Saintyves et al., 2020; Teng et al., 2022). Experimental studies have

begun to probe these effects, but systematic mapping of parameter space in confined Stokes flow environments remains limited.

This thesis addresses this gap by investigating the motion of finite-length cylinders near walls under varying degrees of confinement in the low-Reynolds-number regime. Combining numerical simulation with analytical scaling arguments, the study examines how confinement geometry modifies hydrodynamic resistance, torque generation, and translation–rotation coupling, with a particular focus on identifying the conditions under which slipping or forward motion occurs. The results contribute to a more complete understanding of near-wall hydrodynamics in realistic three-dimensional environments, with implications for both biological systems and engineered microscale devices.

1.1 Literature Review

In microscale fluid mechanics, many flows occur in the low-Reynolds-number regime, where viscous forces dominate over inertia, the governing Stokes equations are linear, and the motion is reversible under time reversal (Happel & Brenner, 1983; Leal, 2007; Stokes, 2009). In this regime, the presence of nearby boundaries plays a decisive role in determining particle dynamics (Jeffrey & Onishi, 1981; Mitchell & Spagnolie, 2015; O'Neill, 1964). Walls break the symmetry of the surrounding flow, leading to increased hydrodynamic drag, changes in far-field decay rates, and coupling between translational and rotational motion (Gavze & Shapiro, 1997; Goldman, Cox & Brenner, 1967; Katz et al., 1975; Koens & Montenegro-Johnson, 2021; Rallabandi, Saintyves, Jules, Salez, Schönecker, Mahadevan & Stone, 2017; Spagnolie & Lauga, 2012; Teng et al., 2022). These near-wall effects occur regardless of whether the moving body is a sphere, cylinder, or more complex shape. They are a universal feature of microscale hydrodynamics across both natural and engineered systems (Crowdy, 2011; Ishimoto & Gaffney, 2013; Zhu et al., 2013).

The effects introduced by walls and confinement have critical importance across a wide range of application fields. For example, they govern the swimming patterns of microorganisms in confined habitats, influence the efficiency and precision of microrobotic navigation (Acemoglu & Yesilyurt, 2015; Caldag & Yesilyurt, 2019; Lauga et al., 2006; Spagnolie & Lauga, 2012; Zhu et al., 2013), dictate wear and performance in MEMS de-

vices(Choi et al., 2010; Day & Stone, 2000; Sen et al., 1996; Witelski, 1998), and control transport processes in colloidal suspensions and microfluidic devices (Abel et al., 1994; Choi et al., 2010; Dong, Lum, Hu, Zhang, Ren, Onck & Sitti, 2020; Leal, 2007; Mitchell & Spagnolie, 2015). As such, understanding how objects move near walls is a central challenge in microhydrodynamics, with implications extending from the fundamental physics of viscous flows to the design of next-generation biomedical and industrial technologies.

In biological systems, many microorganisms navigate near solid boundaries, where hydrodynamic wall interactions significantly modify their swimming kinematics and stability (Spagnolie & Lauga, 2012). These interactions can induce behaviors such as circular swimming, accumulation near surfaces, and reorientation of swimming direction, all arising from the coupling between the organism's propulsive mechanism and the hydrodynamic image systems generated by the boundary (Crowdy, 2011; Ishimoto & Gaffney, 2013; Lauga et al., 2006; Spagnolie & Lauga, 2012). For example, pusher-type swimmers such as *Escherichia coli* generate thrust from the rear via rotating helical flagellar bundles (Das & Lauga, 2018; Lauga et al., 2006; Spagnolie & Lauga, 2012), creating a net hydrodynamic torque in the presence of a no-slip wall that drives persistent circular trajectories (Lauga et al., 2006; Zöttl & Stark, 2012). Sperm cells and other flagellated swimmers similarly experience wall-induced reorientation and trapping, phenomena captured in multipole models and slender-body simulations that link near-wall attraction to the strength and orientation of force dipoles and higher-order hydrodynamic singularities (Ishimoto & Gaffney, 2013; Koens & Montenegro-Johnson, 2021; Spagnolie & Lauga, 2012). Ciliated protozoa such as *Paramecium* propel themselves via coordinated nonreciprocal ciliary beating, where metachronal wave patterns can be tuned to enhance net flow generation and surface-bound locomotion (Dong et al., 2020; Ishimoto & Gaffney, 2013). The resulting dynamics are strongly geometry-dependent: variations in cell shape, flagellar arrangement, and beating kinematics determine whether a swimmer behaves as a puller, pusher, or neutral type, which in turn dictates its stability and accumulation behavior near boundaries (Daddi-Moussa-Ider et al., 2021; Ishimoto & Gaffney, 2013; Spagnolie & Lauga, 2012). These hydrodynamic mechanisms, often supplemented by steric and lubrication forces in the near-field (Happel & Brenner, 1983; Leal, 2007; Salez & Mahadevan, 2015), underpin a wide range of biological functions, including microbial navigation toward nutrient-rich surfaces, sperm guidance in reproductive tracts, and ciliate-mediated feeding currents in aquatic environments.

Artificial microswimmers designed for biomedical applications, such as targeted drug delivery, minimally invasive surgery, and in-situ diagnostics, often operate in confined microchannel environments where wall effects play a decisive role in their propulsion and

guidance (Acemoglu & Yesilyurt, 2015; Caldag & Yesilyurt, 2019). Magnetic helical microrobots, inspired by bacterial flagella, generate propulsion through the rotation of a rigid helical tail actuated by an external magnetic field, with swimming speed and trajectory stability determined by the balance between magnetic and viscous torques at low Reynolds number (Acemoglu & Yesilyurt, 2015; Caldag & Yesilyurt, 2019; Das & Lauga, 2018). In cylindrical channels, confinement modifies the hydrodynamic resistance matrix, altering both translational and rotational velocities; these effects can be exploited to achieve controlled steering by adjusting actuation frequency or magnetic field orientation (Acemoglu & Yesilyurt, 2015; Zhu et al., 2013). However, the same near-wall hydrodynamic interactions that enable guided motion can also produce unintended drift, circular trajectories, or trapping, particularly for pusher-type swimmers whose head–tail counter-rotation generates lateral hydrodynamic torques in proximity to boundaries (Lauga et al., 2006; Spagnolie & Lauga, 2012). Numerical and experimental studies have shown that confinement geometry, channel diameter, and tail length significantly influence stability, with narrow channels enhancing alignment along the channel axis while also increasing susceptibility to step-out or wobbling instabilities at suboptimal actuation parameters (Acemoglu & Yesilyurt, 2015; Caldag, Acemoglu & Yesilyurt, 2017; Caldag & Yesilyurt, 2019; Zöttl & Stark, 2012). The ability to predict and harness these wall-mediated dynamics is critical for designing microrobotic systems capable of reliable navigation through vascular networks, microfluidic devices, and other constrained environments relevant to precision therapeutic delivery.

In MEMS devices, where moving components operate within micron-scale gaps, hydrodynamic lubrication fundamentally governs performance and stability (Happel & Brenner, 1983; Leal, 2007). In such confined geometries, the proximity of walls amplifies viscous resistance and alters pressure distributions, directly influencing drag, dissipation, and overall efficiency (Choi et al., 2010; Day & Stone, 2000). Devices such as rotary actuators, viscous micropumps, and air-bearing sliders rely on precise lubrication-film characteristics to maintain performance (Day & Stone, 2000; Sen et al., 1996; Witelski, 1998). In rotary-cylinder micropumps, lubrication theory predicts strong coupling between torque, flow rate, and pressure drop at small clearances, with eccentric placement enabling controllable pumping or motoring depending on rotation direction (Choi et al., 2010; Day & Stone, 2000; Sen et al., 1996). Analytical models further show that design trade-offs, throughput, and rotational speed cannot be maximized simultaneously (Choi et al., 2010; Day & Stone, 2000). Similarly, in high-speed air-bearing sliders for data storage, compressible lubrication flows generate lift that balances applied loads, and stability arises from nonlinear interactions between bearing geometry and gap pressure fields (Witelski, 1998). At the nanoscale flying heights of these devices, compressibility

and side-leakage effects become decisive (Witelski, 1998). Across these systems, even slight deviations in alignment or clearance can shift force balances, tipping the system between smooth operation and contact (Choi et al., 2010; Day & Stone, 2000)

In colloidal suspension and microfluidic systems, hydrodynamic interactions with nearby boundaries are often the dominant factor governing particle sedimentation, translation, and rotation. At low Reynolds numbers, these wall-mediated effects arise from the alteration of disturbance flows and the amplification of lubrication stresses (Mestre, 1973; Salez & Mahadevan, 2015), which modify drag coefficients, influence particle alignment, and, under certain conditions, generate hydrodynamic trapping. Classical analyses, such as De Mestre *et al.*'s treatment of slender cylinders settling near plane boundaries, quantify wall-correction factors for drag and reveal that orientation stability is generally lost except for specific geometric configurations (Mestre, 1973). More recent studies extend these insights to confined geometries relevant for lab-on-a-chip applications, where nonlinear hydrodynamic coupling between translation and rotation leads to complex accumulation patterns and sorting dynamics (Mitchell & Spagnolie, 2015). Rallabandi *et al.* (Rallabandi et al., 2017) demonstrated that wall-induced coupling between rotational and translational motion can be tuned to control particle orientation and lateral drift, forming the basis for passive hydrodynamic sorting and trapping strategies in microfluidic environments. Bioinspired designs, such as cilia-driven flows, create recirculating zones that selectively retain or expel particles based on size, motility, or surface properties, offering additional control over sorting efficiency (Dong et al., 2020). Optimal control frameworks similarly exploit wall-induced hydrodynamic torques to achieve high-efficiency positioning and separation of both passive particles and active swimmers (Spagnolie & Lauga, 2012). These mechanisms directly support applications in high-throughput biomedical assays (Acemoglu & Yesilyurt, 2015; Caldag & Yesilyurt, 2019), microfluidic sorting and transport, and precision coating flows, where thin-film lubrication and elastohydrodynamic interactions between particles and compliant boundaries can be harnessed to modulate motion and contact forces (Salez & Mahadevan, 2015). As such, the ability to accurately predict and leverage particle–wall interactions remains central to advancing the control and performance of colloidal systems, microfluidic platforms, and next-generation diagnostic technologies.

The theoretical study of hydrodynamic interactions between particles and boundaries at low Reynolds number originates from classical solutions for spheres near walls. Seminal work by O'Neill on the slow viscous motion of a sphere translating parallel to a plane boundary solved the Stokes equations in bispherical coordinates, producing exact expressions for the mobility and resistance coefficients and showing that the parallel drag

increases logarithmically with decreasing gap height (O'Neill, 1964). Complementary analyses for motion parallel to the wall (Goldman et al., 1967) and later extensions to finite confinement provided wall-correction factors that remain standard in microhydrodynamic modeling. These solutions demonstrated that wall proximity modifies not only the magnitude of hydrodynamic forces but also the scaling of resistance with particle–wall separation, laying the groundwork for more complex geometries. The transition from spheres to non-spherical bodies introduced symmetry-breaking effects and additional hydrodynamic coupling between translation and rotation. Jeffery's pioneering analysis of the motion of circular cylinders in viscous fluids (Gavze & Shapiro, 1997; Jeffrey & Onishi, 1981). Subsequent work on the slow motion of a cylinder near a plane wall (O'Neill, 1964) revealed fundamental differences from spheres, including the absence of lateral forces on a steadily rotating cylinder and the lack of torque on a translating one. For slender bodies, Cox's slender-body theory (Cox, 1970) and its extensions incorporated wall effects via singularity methods and Stokeslet image systems, enabling analytical predictions for the mobility of fibers and rods near boundaries(De Mestre & Russel, 1975; Katz et al., 1975; Koens & Montenegro-Johnson, 2021). De Mestre's analysis of the low-Reynolds-number fall of slender cylinders near rigid walls (Mestre, 1973) quantified the drag anisotropy and demonstrated that stable orientations during sedimentation are rare except in narrowly defined configurations. These foundational studies established the primacy of geometry—sphere, cylinder, or slender fiber—in determining mobility and resistance scaling, and they form the analytical backbone for contemporary theories describing near-wall dynamics of complex-shaped passive and active particles (Gavze & Shapiro, 1997; Spagnolie & Lauga, 2012).

The study of cylindrical motion near a single rigid wall at low Reynolds number has its roots in the exact solution of Jeffery (Jeffery & Filon, 1922), who employed bipolar coordinates to calculate the torque on an infinite circular cylinder rotating in a viscous fluid, both in isolation and in proximity to another cylinder or a wall. This analysis provided one of the earliest treatments of wall-induced hydrodynamic coupling in two-dimensional Stokes flow. Building on this foundation, Jeffery & Onishi (Jeffrey & Onishi, 1981) presented a general formulation for the mobility and resistance functions of an infinite cylinder translating or rotating parallel or perpendicular to a nearby plane wall. Their exact solutions, obtained via stream-function representations in bipolar coordinates, revealed qualitative differences from the spherical analogue, such as the absence of a lateral force on a steadily rotating infinite cylinder near a wall, in contrast to the finite force experienced by a sphere. These idealised results remain important benchmarks for validating numerical methods and asymptotic theories in near-wall hydrodynamics.

Two analytical tools have been central to this class of problems. The Lorentz reciprocal theorem allows relations between distinct force–velocity or torque–angular-velocity problems without directly re-solving the governing Stokes equations, enabling the derivation of new mobility and resistance relations from known configurations (Happel & Brenner, 1983; Leal, 2007). Lubrication theory, applied in the limit of small cylinder–wall separation, captures the leading-order pressure gradients and shear stresses in the thin film, predicting the divergence of resistance and torque coefficients with decreasing gap (Koens & Montenegro-Johnson, 2021). The combination of these methods has been extended to account for end effects in finite-length cylinders, where symmetry is broken and rotation–translation coupling becomes significant (Teng et al., 2022), as well as to compliant boundaries, where elastic deformation of a coating modifies the lubrication pressure and can induce additional lift or torque (Rallabandi et al., 2017; Saintyves et al., 2020; Salez & Mahadevan, 2015). Further refinements include analyses of reverse rotation phenomena (Merlen & Frankiewicz, 2011; Seddon & Mullin, 2006) and the motion of immersed cylinders near soft, elastic coatings (Rallabandi et al., 2017), both of which illustrate the sensitivity of near-wall dynamics to boundary material properties. Together, these theoretical developments provide a rigorous framework for interpreting and predicting the hydrodynamics of rigid and flexible cylindrical bodies in the presence of a single boundary, while also serving as the foundation for modern extensions to active and anisotropic particles.

In Stokes flows, translation–rotation coupling arises from the asymmetry introduced when a particle moves in proximity to a boundary, where the disturbance flow interacts with the wall and alters the hydrodynamic resistance matrix. The effect is particularly strong for elongated bodies, where the unequal distribution of hydrodynamic stresses along the body induces rotation during translation, or conversely, lateral drift during pure rotation (Koens & Montenegro-Johnson, 2021; Rallabandi et al., 2017; Teng et al., 2022). In biological systems, such coupling manifests in characteristic near-wall swimming behaviors. For example, pusher-type bacteria such as *E. coli* generate rear-mounted thrust that, in the presence of a no-slip wall, produces a net torque driving persistent circular trajectories (Das & Lauga, 2018; Lauga et al., 2006; Spagnolie & Lauga, 2012). Similarly, slender-body and multipole models predict that wall-mediated hydrodynamic coupling reorients swimmers and can lead to stable trapping, depending on the strength and orientation of the force dipoles (Spagnolie & Lauga, 2012; Zhu et al., 2013). In synthetic systems, microrobots driven by rotating helical tails experience analogous coupling effects: translation generates rotation and vice versa, enabling passive steering in confined geometries but also making them susceptible to unintended drift or alignment shifts (Acemoglu & Yesilyurt, 2015; Caldag & Yesilyurt, 2019). Across both natural and engineered

microswimmers, understanding and exploiting translation–rotation coupling is essential for predicting near-wall trajectories and designing systems that can either harness or suppress these hydrodynamic interactions, depending on the application.

In microscale hydrodynamics, confinement refers to the modification of particle motion by nearby boundaries that restrict the surrounding fluid domain. Geometries can range from a single plane wall to two parallel plates, cylindrical channels, or fully enclosed cavities, each imposing distinct hydrodynamic constraints. Confinement alters both translational and rotational mobilities by modifying the disturbance flow fields and amplifying wall-mediated lubrication stresses. For cylinders, these effects are captured in theoretical and computational models that incorporate wall-correction factors into the hydrodynamic resistance matrix, revealing pronounced increases in drag and altered translation–rotation coupling at small gap ratios (Mitchell & Spagnolie, 2015; Teng et al., 2022). In compliant-walled systems, additional coupling arises from elastohydrodynamic deformations, as described by lubrication theory for soft interfaces (Salez & Mahadevan, 2015), where wall compliance can either enhance or diminish resistance depending on geometry and material properties. Such modifications to mobility are not merely quantitative; they can induce qualitative changes in particle dynamics, including trajectory reorientation, alignment along symmetry axes, and confinement-induced trapping, with direct implications for microfluidics, MEMS operation, and targeted microrobotic navigation.

Rotation in confined geometries exhibits behaviors absent in unbounded Stokes flow, including spontaneous reverse motion. This effect arises from asymmetries in the lubrication layer thickness and the resulting pressure gradients, which generate hydrodynamic torques capable of reversing or altering rotation direction.Teng et al. (2022) demonstrated, using three-dimensional lubrication theory, that finite-length cylinders near walls exhibit end effects that fundamentally change their rotational dynamics under confinement. Saintyves et al. (2020) experimentally observed rotation–translation coupling in cylinders sedimenting in narrow gaps, identifying asymmetric pressure distributions in the lubrication film as the primary mechanism for induced rotation. Similarly, Seddon & Mullin (2006) reported reverse rotation of cylinders in narrow channels, where geometric confinement and lubrication asymmetry combined to produce motion opposite to that expected from unconfined hydrodynamics.

The geometry of confinement not only determines the magnitude of hydrodynamic resistance but also introduces directional anisotropy, where mobility coefficients differ significantly along orthogonal directions. Cylindrical particles translating parallel to channel walls experience markedly different resistance compared to motion perpendicular to them, a trend amplified as the gap-to-radius ratio decreases (Gavze & Shapiro, 1997; Mitchell &

Spagnolie, 2015). Variations in confinement geometry, such as replacing rigid walls with compliant boundaries, can further modify near-wall hydrodynamics through wall deformation, altering flow topology and lubrication pressures (Salez & Mahadevan, 2015). In background shear flows, confinement can enhance or suppress lateral migration depending on the interplay between shear-induced lift forces and wall-mediated lubrication stresses (Zöttl & Stark, 2012). These sensitivities to gap ratio, wall compliance, and imposed background flows make accurate geometric characterization essential for predicting motion in both natural and engineered microscale systems.

1.2 Motivation

Across a broad range of disciplines, from microbiology and colloid science to MEMS design and microrobotics, near-wall hydrodynamics has emerged as a central factor in predicting and controlling motion at low Reynolds numbers. Theoretical frameworks, supported by both analytical and numerical studies, have provided deep insights into wall-mediated resistance, translation–rotation coupling, and confinement-induced modifications to mobility. However, much of this foundational work has been carried out under idealised assumptions, such as infinite-length bodies, single rigid walls, two-dimensional symmetry, or axisymmetric flows (Czajka et al., 2019; Jeffrey & Onishi, 1981; Rallabandi et al., 2017). While these simplifications enable analytical progress, they often neglect geometric and boundary complexities encountered in real-world systems, including finite-body effects, end interactions, and multi-wall confinement.

Despite significant advances, relatively few studies address the fully three-dimensional motion of *finite-length* cylinders in confined Stokes flow, where all three spatial dimensions contribute to hydrodynamic resistance and coupling. In particular, the onset and character of *slipping*, a regime in which a rotating body exhibits net translation without external forcing, remain poorly mapped as a function of confinement ratio and gap geometry (Saintyves et al., 2020; Teng et al., 2022). The interplay between lubrication-layer asymmetry, end effects, and multi-wall interactions in such settings is not well resolved in the existing literature. This thesis addresses this gap through a combined numerical and parametric approach, systematically mapping cylinder motion across a range of confinement scenarios (channel, open tank, closed tank) and identifying the hydrodynamic mechanisms governing the transition between pure rotation, slipping, and translation-

dominated regimes.

1.3 Thesis Outline

This thesis investigates low–Reynolds–number motion of a cylinder near a wall under three confinement types (channel, closed tank, open tank) in both 2-D (infinite) and 3-D (finite-length) settings. Chapter 1 motivates the problem and frames the role of confinement in near-wall microhydrodynamics. Chapter 2 provides a review of the existing theory on infinite and finite-length cylinders near a wall in an unbounded domain. Chapter 3 introduces the geometry and boundary conditions, presents the governing equations, and outlines the finite-element implementation and validation. Chapter 4 reports how gap size, aspect ratios, and confinement scenario affect the direction and magnitude of motion in 2-D and 3-D, and decomposes forces into cap vs. side contributions and pressure- vs. shear-driven components. Chapter 5 concludes with the main findings on how confinement sets translation direction and magnitude, and summarizes the mechanistic picture that links side pressure and shear with end-cap effects.

2. THEORETICAL BACKGROUND

Understanding the hydrodynamic behavior of cylindrical bodies near boundaries requires a theoretical framework that captures the interplay between viscous forces, geometric confinement, and wall interactions in the low Reynolds number regime. Theoretical models based on Stokes flow and lubrication theory have long served as the foundation for analyzing such systems, offering insights into the forces and torques experienced by translating and rotating bodies. This chapter reviews the canonical solutions for infinite cylinders near rigid planar walls and extends the discussion to include more recent developments that account for end effects, wall deformability, and finite-length geometries.

2.1 Flow over an Infinite Cylinder Near a Wall

In his 1922 paper, Jeffery & Filon (1922) presented an analytical solution for the motion of a viscous fluid between two non-concentric rotating cylinders by employing bipolar coordinates. He solved the biharmonic equation governing two-dimensional steady viscous flow and derived the stream function for configurations in which one cylinder encloses the other. Jeffery & Filon (1922) showed that steady flow is only possible when one cylinder is enclosed by another. If both cylinders are placed in an infinite fluid, a steady flow cannot be maintained because the fluid motion spreads out without limit. He also calculated the torque per unit length required to maintain the rotation of the inner cylinder in both enclosed and semi-infinite domains. Jeffery's work is notable for its rigorous use of bipolar coordinates and for laying the groundwork for the study of rotational motion in low-Reynolds-number hydrodynamics. Building upon this, Jeffrey & Onishi (1981) extended the analysis to more complex boundary conditions by considering a cylinder near a plane wall. While Jeffery & Filon (1922) focused on confined flows between two

cylinders, the later study reformulated the bipolar coordinate system to model a cylinder adjacent to a planar boundary, treating the wall as a limiting case of a concentric outer cylinder of infinite radius. This reformulation enabled an analytical solution for Stokes flow under three distinct motion types: rotation of the cylinder, translation parallel to the wall, and translation perpendicular to the wall.

A key insight of their work was the decoupling of force and torque under certain constraints: a rotating cylinder experiences no net translational force, and a translating cylinder experiences no net torque. These results, which contrast with the behavior of a sphere in similar settings, demonstrate that the coupling between translational and rotational motion can vanish in planar geometries. The authors provided explicit expressions for the forces and torques in each scenario and further validated their findings using lubrication theory in the near-wall limit.

Theory is formulated as highly dependent on the ratios in the geometry (Figure 3.1), so we start with defining $\delta_{wall} = h_0/R$, where h_0 is the minimum gap height between the cylinder and the wall and R is the radius of the cylinder. The viscosity of the fluid medium is μ, and the rotational and translational velocity of the cylinder parallel to the wall is defined as Ω and U, respectively. Using these parameters, Jeffrey & Onishi Jeffrey & Onishi (1981) showed that the non-dimensional force (non-dimensionalised by μU) over the cylinder when translating next to a wall is defined as:

$$f_{\parallel} = -4\pi \log\left(1 + \delta_{\text{wall}} + \sqrt{2\delta_{\text{wall}} + \delta_{\text{wall}}^2}\right)^{-1} \tag{2.1}$$

Additionally, they solved for the torque per unit length (non-dimensionalised by $\mu\Omega R^2$) of the cylinder that is rotating next to the wall with the velocity Ω as:

$$\tau = -4\pi \frac{1 + \delta_{\text{wall}}}{\sqrt{2\delta_{\text{wall}} + \delta_{\text{wall}}^2}} \tag{2.2}$$

These expressions show how the hydrodynamic interactions intensify as the cylinder approaches the wall (i.e., as $\delta_{wall} \to 0$), and they reveal decoupling behaviors, such as zero torque during translation and zero force during rotation—contrasting with the behavior of spheres.

While the primary focus of this thesis is on parallel translation and rotation near bound-

aries, the solution for the translation of a cylinder perpendicular to wall is worth noting. Although not directly relevant to the present analysis, this case is included here to provide a more complete overview of near-wall hydrodynamic behavior at low Reynolds numbers.

This configuration introduces a strong geometric dependence, captured by the dimensionless gap ratio $\delta_{\text{wall}} = h_0/R$, where h_0 is the minimum wall-cylinder distance and R is the cylinder radius. Jeffery & Onishi derived the non-dimensional force acting on the cylinder (scaled by μV), where V is the speed of translation away from the wall, as

$$f_\perp = -4\pi \left[\log\left(1 + \delta_{\text{wall}} + \sqrt{2\delta_{\text{wall}} + \delta_{\text{wall}}^2}\right) - \frac{\sqrt{2\delta_{\text{wall}} + \delta_{\text{wall}}^2}}{1 + \delta_{\text{wall}}} \right]^{-1},$$

This expression reveals a logarithmic singularity as the gap narrows, indicating a sharp increase in resistance to motion. The result is particularly relevant in modeling sedimentation or lift-off dynamics and complements the parallel translation and rotation cases by completing the set of canonical motions near a boundary.

Additional studies by Ray Ray (1936) and Davis (1993) extended the analysis to generalized resistance coefficients for disk-shaped bodies. While these contributions are not directly applicable to the current study, they are noted here for completeness within the broader context of low-Reynolds-number hydrodynamics.

2.2 Flow over a Finite Cylinder

This study examines both infinite and finite-length cylinders, making it necessary to consider theoretical models that account for end effects. Among these, the work of Teng et al. (2022) is particularly relevant. Their three-dimensional lubrication theory describes the coupled translation and rotation of finite-length cylinders near rigid planar walls and was motivated by the experimental findings of Saintyves et al. (2020). While Saintyves et al. (2020) focused on soft substrates and elastohydrodynamic effects, Teng et al. (2022) extended the framework to rigid boundaries, isolating the role of geometric confinement.

An earlier study by Rallabandi et al. (2017) laid the theoretical groundwork by investigating the spontaneous rotation of an infinite cylinder sliding near a soft elastic wall in a viscous fluid. Using a two-dimensional model under low Reynolds number conditions,

they employed lubrication theory and the Lorentz reciprocal theorem to derive analytical expressions for the cylinder's angular velocity, showing that it scales with the cube of the sliding speed and the square of the wall's elastic deformation. These predictions were validated through numerical simulations solving the Reynolds lubrication equation to capture the pressure and torque distributions. The results revealed that wall deformation breaks flow symmetry, generating a lift force and inducing torque-free rotation. Notably, the study bridges theoretical predictions with experimental observations of buoyancy-driven rotation on soft inclines, offering valuable insights into elastohydrodynamic interactions.

Inspired by this foundational work, Saintyves et al. (2020) extended the investigation to finite-length cylinders, which are more representative of real-world systems. The theory of Rallabandi et al. (2017) predicted that a cylinder sliding parallel to a soft wall must experience spontaneous rotation in the absence of external torque—analogous to frictional rolling in rigid body mechanics—due to symmetry-breaking in the pressure field caused by wall deformation. However, this theory showed quantitative discrepancies when compared with experimental results. To address this issue, Saintyves et al. (2020) developed a composite theoretical model that incorporates both the elastohydrodynamic torque along the cylinder's curved surface and a newly identified viscous torque arising from friction at the cylinder's ends, highlighting the critical role of end effects in finite-length cylinder motion. They derived scaling laws that predict the angular velocity as a sum of contributions from both mechanisms and validated these predictions through a series of controlled experiments. Using aluminum and brass cylinders of varying aspect ratios, immersed in silicone oil and sliding down soft polymer-coated inclines, they systematically varied the polymer coating's stiffness, thickness, and incline angle. High-resolution imaging and particle tracking allowed precise measurement of rotation and translation speeds. The results showed a clear transition from edge-effect-dominated rotation in short cylinders or stiff coatings to coating deformation-dominated rotation in longer cylinders or softer coatings. This comprehensive approach not only confirmed the qualitative predictions of the theory of Rallabandi et al. (2017) but also provided a quantitative framework for understanding motion near soft boundaries.

Motivated by discrepancies observed in experiments on finite-length cylinders sliding near soft inclines Saintyves et al. (2020), Teng et al. (2022) developed a three-dimensional lubrication theory to describe the coupled translation and rotation of finite-length cylinders near rigid planar walls. Unlike classical models for infinite cylinders, their approach explicitly incorporates end effects, which are crucial for capturing the coupling between force and torque. By applying the Lorentz Reciprocal Theorem within the lubrication region, they converted complex surface integrals into more tractable line integrals, allowing for

analytical expressions of hydrodynamic force and torque. Solving the Reynolds equation under these constraints and incorporating corrections from flow outside the lubrication region, they derived the following expressions for force and torque:

$$\hat{\mathbf{F}} = -\frac{2\pi\mu\hat{U}lL}{h_0}\mathbf{e}_x - \frac{3\pi\mu\hat{V}l^3L}{2h_0^3}\mathbf{e}_z, \quad \hat{\mathbf{T}} = -\frac{2\pi\mu R\hat{\Omega}lL}{h_0}\mathbf{e}_y, \tag{2.3}$$

Subsequently, Teng et al. (2022) isolate the individual contributions of translation and rotation to the hydrodynamic force and torque by solving the lubrication equations under distinct motion conditions. By incorporating the influence of flow outside the lubrication layer and leveraging the linearity of Stokes flow, they superimpose these solutions to construct a unified expression. This leads to a compact resistance matrix formulation that captures the coupled dynamics of finite-length cylinders translating and rotating near a rigid wall as follows:

$$\begin{bmatrix} F \\ T \end{bmatrix} = \begin{bmatrix} R^{FU} & R^{F\Omega} \\ R^{TU} & R^{T\Omega} \end{bmatrix} \begin{bmatrix} U \\ \Omega \end{bmatrix} \tag{2.4}$$

The terms $R^{F\Omega}$ and R^{TU} are cross-coupling resistance coefficients that arise due to the presence of end effects in finite-length cylinders. These coefficients are absent in classical formulations such as Jeffery & Filon (1922), which assume infinite cylinders and therefore neglect end-induced interactions. However, coupling between translation and rotation does occur in spherical or finite geometries, as demonstrated in both experimental and numerical studies. Due to the symmetry of Stokes flow, these cross-coupling terms are mathematically identical, as noted by Hinch (1972). In contrast, the diagonal resistance coefficients R^{FU} and $R^{T\Omega}$ also incorporate end effects but represent the direct hydrodynamic resistance to translation and rotation, respectively. All of these resistance terms depend on the integral that captures the influence of the lubrication pressure distribution and varies with both the gap height and the cylinder's aspect ratio.

3. METHODOLOGY

This chapter outlines the numerical and theoretical framework employed to investigate the low-Reynolds-number behavior of a rigid cylinder near a planar boundary under varying confinement conditions. The approach combines analytical assumptions under the Stokes regime with high-fidelity finite element simulations using COMSOL Multiphysics. The study involves both two- and three-dimensional configurations to isolate the role of end effects and geometric confinement on hydrodynamic coupling between rotation and translation. The subsequent sections describe the problem formulation, boundary and motion constraints, governing equations, numerical setup, and validation strategy.

3.1 Problem Definition

In creeping flow regimes, even simple geometric configurations can give rise to complex hydrodynamic behavior due to the dominance of viscous forces and the influence of nearby boundaries. One such configuration is a rigid cylinder near a planar wall, where the coupling between translational and rotational motion is sensitive to geometric confinement. While classical theory suggests that a force-free rotating infinite cylinder does not translate, and a torque-free translating cylinder does not rotate, the presence of nearby walls and a three-dimensional environment with a finite length cylinder introduces end effects that break this decoupling.

This study investigates the hydrodynamic behavior of a rigid cylinder placed near a planar wall inside a viscous, incompressible fluid. The objective is to understand how varying degrees and types of geometric confinement influence the forces and torques acting on the cylinder, particularly under prescribed rotation. Two boundary conditions are applied to the cylinder. First, a force-free condition, in which a rotational velocity is prescribed

while the net hydrodynamic force is constrained to zero. Second, a fixed condition, where the cylinder is rotated at a constant angular velocity without translation, allowing a net hydrodynamic force to develop.

The effect of confinement is studied across three scenarios: channel, open tank, and closed tank geometries. Both 2D and 3D cases are examined to evaluate the role of dimensionality and end effects. In 3D, the length-to-diameter ratio and wall proximity are varied to assess back-wall influence, while in 2D, aspect ratios between the bounding boxes width and height and gap height are systematically studied to optimize the region of interest before extending to 3D. The study aims to map the dependence of force-torque coupling and slipping motion on confinement geometry, providing insight into low-Reynolds-number transport and near-wall motion in microfluidic environments.

To guide the reader through the range of simulations conducted, a table summarizing all of the simulations is provided in Table 3.1. It summarizes the different configurations studied, categorized by dimensionality, motion constraints, and confinement geometry.

Table 3.1 Summary of simulation cases across dimensionality, motion type, and confinement geometry, including key geometric parameters.

Dimensionality	**Motion Type**	**Confinement**	**Varied Parameters**
2D	Force-Free	Channel Open Tank Closed Tank	W_x/W_z, d_{wall}
	Fixed	Channel Open Tank Closed Tank	W_x/W_z, d_{wall}
3D	Force-Free	Channel Open Tank Closed Tank	L, W_y
	Fixed	Channel Open Tank Closed Tank	L, W_y

Although two distinct boundary conditions are applied to the cylinder, force-free and fixed, the resulting dynamics are evaluated jointly within each confinement scenario (Channel, Open Tank, and Closed Tank). Rather than treating these conditions separately, forces, torques, and velocities of the cylinders are analyzed together to provide a more holistic understanding of near-wall hydrodynamics. This integrated approach enables direct comparisons and highlights the physical interplay between translation and rotation under geometric confinement.

3.1.1 Geometry

A finite-length cylinder with a unit diameter $D = 2R = 1$ (set to unity for non-dimensionalisation purposes) and length L is placed inside a rectangular domain with dimensions W_x, W_y, and W_z. The cylinder is placed at the geometric center of the xy-plane, with a minimum gap height from the bottom wall denoted by d_{wall}. To reduce computational cost and take advantage of the symmetry of the geometry, a symmetry condition is applied on the xz plane. Forces in the y-direction are zero due to symmetry, and the forces in the z-direction are neglected. The cylinder rotates only about the y-axis with angular velocity Ω, and translates only in the x-direction with velocity U. The rotation frequency is set to unity, $f = 1$, corresponding to an angular velocity of $\Omega = 2\pi$. The characteristic velocity scale used in the non-dimensionalization is defined as $\tilde{U} = \tilde{f}\tilde{D}$, where tildes denote dimensional quantities.

To investigate the effects of confinement in both axial and transverse directions, simulations were conducted in both two- and three-dimensional domains. The two-dimensional simulations represent the idealized limit of an infinitely long cylinder and were used to perform extensive parametric sweeps across the wall gap height d_{wall} and domain aspect ratios W_x/W_z. To capture the full range of near-wall hydrodynamic interactions, simulations were conducted for dimensionless wall distances d_{wall} spanning five orders of magnitude, from 10^{-1} to 10^{-6}. Between 0.1 and 0.01, the values were sampled using linear decrements of 0.01. From 0.01 to 0.001, the spacing was reduced to uniform steps of 0.001. Below 0.001, the sampling was further refined with progressively smaller increments—typically 1×10^{-4} to 1×10^{-5}—and extended logarithmically down to $d_{\text{wall}} = 1 \times 10^{-6}$. This adaptive spacing strategy ensured sufficient resolution near contact, where steep gradients in force and velocity occur due to lubrication effects. Aspect ratios in the range of 0.5 to 6 were selected, as this interval was found to sufficiently capture the transitions in the direction of cylinder motion under varying confinement conditions. The domain width W_x and height W_z values for their respective aspect ratios are presented in Table 3.2.

Table 3.2 Aspect ratios considered in 2D simulations and their corresponding non-dimensionalised domain lengths.

Aspect Ratio (W_x/W_z)	Domain Width (W_x)	Domain Height (W_z)
0.5	20	40
2	40	20
3	15	5
6	30	5

Evaluation of these 2D cases offered a computationally efficient way to explore a broad parameter space and to inform the design of more computationally intensive 3D simulations.

Based on insights obtained from the two-dimensional simulations, appropriate values for the aspect ratio and the minimum wall distance d_{wall} were selected to guide the three-dimensional study. Since the primary objective of this investigation is to characterize the conditions under which backward slipping occurs, d_{wall} was fixed at 0.05, and an aspect ratio of 3 was chosen. Accordingly, a bounding box with dimensions $W_x = 35$, $W_z = W_x/3$, and a variable W_y was constructed, with the cylinder positioned at the geometric center of the domain.

The cylinder was assigned a finite length L, and both the cylinder length and the domain depth W_y were systematically varied to explore the effects of axial confinement and proximity to the back wall. Specifically, L was varied across four representative values, $L = 0.5,\ 1,\ 3,\ 6$, to capture behavior ranging from short, disk-like bodies to elongated cylinders. Simultaneously, domain depths of $W_y = 7,\ 10,\ 30$ were used to evaluate how the clearance between the cylinder and the back wall influences the resulting motion. This configuration enabled a comprehensive assessment of how confinement in all directions modulates the hydrodynamic interactions and the dynamics of the cylinder.

A schematic view of the three-dimensional simulation setup is shown in Figure 3.1.

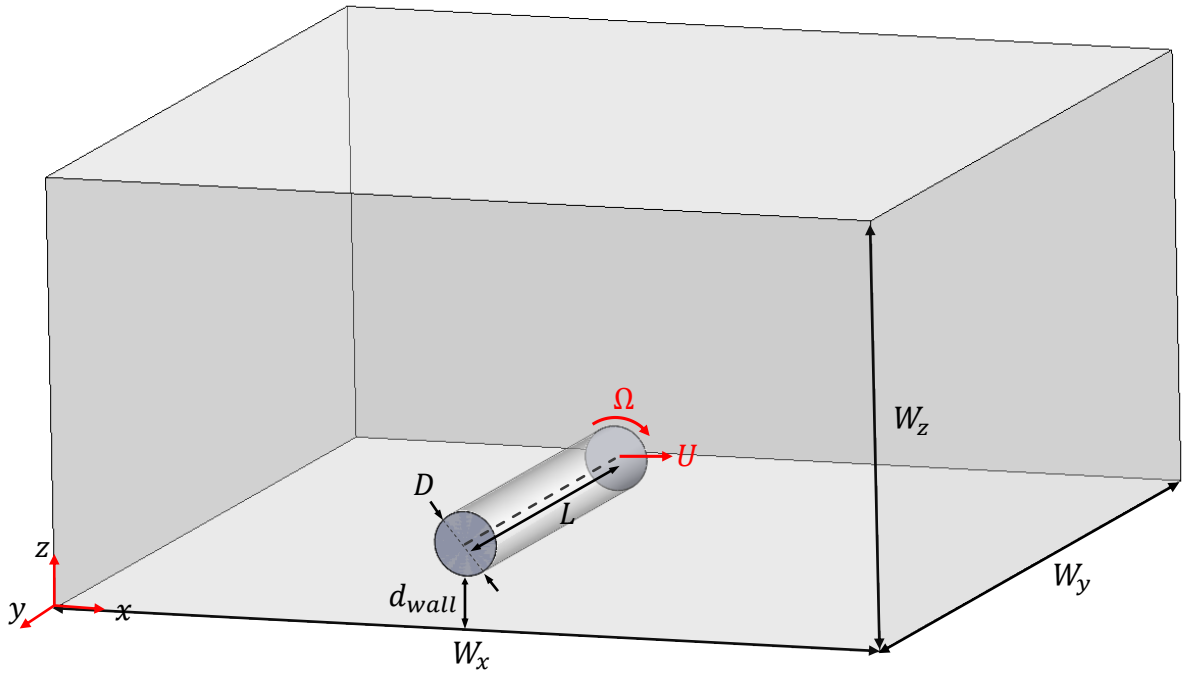

Figure 3.1 Schematic representation of the 3-D computational domain.

3.1.2 Boundary Conditions

To analyze the effect of the confinement on the cylinder's motion, appropriate boundary conditions were applied to both the bounding box and the cylinder. These conditions are categorized based on the confinement scenarios of the domain and the mobility and force constraints imposed on the cylinder.

3.1.2.1 Boundary Conditions of the Bounding Box

The domain boundary conditions were defined according to three distinct confinement scenarios: *Channel Mode*, *Open Tank Mode*, and *Closed Tank Mode*. These configurations were designed to mimic varying degrees of confinement that the cylinder can experience. In all scenarios, the bottom wall of the domain and the surface of the cylinder were assigned no-slip boundary conditions, ensuring zero velocity at those interfaces as well as the back wall of the computational domain for the three-dimensional cases.

Three different confinement configurations were employed: In Channel Mode, the left and right boundaries are stress-free, the top is no-slip, and the bottom is a no-slip wall, aiming to simulate a flow channel with partial confinement, much like a micro pump. In Open Tank Mode, only the top boundary is open (stress-free), while the other walls are no-slip. This setup represents a fluid-filled tank open to the atmosphere. In Closed Tank Mode, all boundaries are no-slip, fully enclosing the domain and simulating a sealed environment.

Figure 3.2 shows a schematic of the domain with corresponding boundary condition assignments for each mode. The table alongside provides a summary of the boundary conditions applied to the vertical walls in the 2D projection.

3.1.2.2 Boundary Conditions of the Cylinder

The cylinder's surface was treated as a no-slip wall in all cases, with two primary motion constraints depending on the simulation mode: the *force-free* case and the *fixed* case.

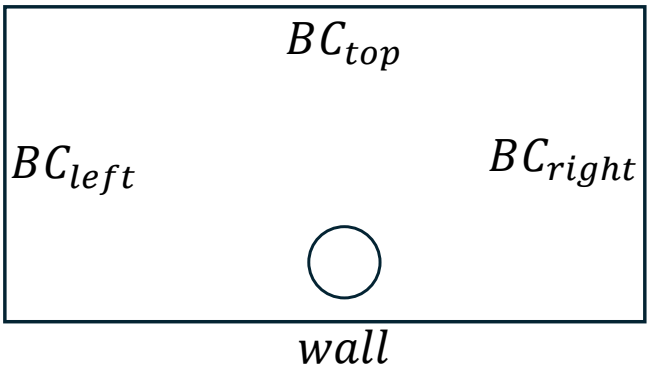

(a) Schematic representation of the boundary conditions.

Confinement	BC_{left}	BC_{top}	BC_{right}
Channel	$\sigma \cdot \mathbf{n} = 0$	$\mathbf{u} = 0$	$\sigma \cdot \mathbf{n} = 0$
Open Tank	$\mathbf{u} = 0$	$\sigma \cdot \mathbf{n} = 0$	$\mathbf{u} = 0$
Closed Tank	$\mathbf{u} = 0$	$\mathbf{u} = 0$	$\mathbf{u} = 0$

(b) Summary of boundary conditions applied to each wall for the confinement cases.

Figure 3.2 Overview of 2-D confinement boundary conditions.

In the force-free configuration, the cylinder was allowed to translate in the x-direction while rotating about the y-axis. The translational velocity U was determined implicitly by enforcing a zero net hydrodynamic force in the x-direction. This condition is particularly relevant under creeping flow assumptions, where inertial effects are negligible and motion is governed primarily by viscous forces.

In the fixed configuration, the cylinder was constrained to pure rotation about its axis, with no translational motion. In both cases, due to symmetry and the imposed boundary conditions, motion in the y and z-directions was neglected.

The general surface velocity of the rotating and translating cylinder can be described as:

$$\mathbf{u} = \begin{bmatrix} U \\ 0 \\ 0 \end{bmatrix} + \begin{bmatrix} 0 \\ \Omega \\ 0 \end{bmatrix} \times \begin{bmatrix} x - x_0 \\ y - y_0 \\ z - z_0 \end{bmatrix}$$

Here, (x_0, y_0, z_0) denotes the geometric center of the cylinder. Due to symmetry and the assumptions outlined above, the translational velocities in the y- and z-directions (V and W), as well as the angular velocities about the x- and z-axes (ω_x and ω_z), are set to zero. As a result, the surface velocity expression simplifies. In the force-free case, the cylinder translates in the x-direction to maintain zero net hydrodynamic force, yielding

the velocity field.

$$\mathbf{u} = \begin{bmatrix} U + \Omega(z - z_0) \\ 0 \\ -\Omega(x - x_0) \end{bmatrix}$$

In the fixed case, the cylinder is not permitted to translate and is only allowed to rotate about the y-axis, leading to the surface velocity

$$\mathbf{u} = \begin{bmatrix} \Omega(z - z_0) \\ 0 \\ -\Omega(x - x_0) \end{bmatrix}$$

These velocity boundary conditions, along with the lubrication regime characterized by a small gap $d_{wall} \ll R$, allow the application of near-wall hydrodynamic approximations such as those introduced by Teng et al. (2022).

3.2 Governing Equations

This section outlines the mathematical framework used to describe the motion of a viscous fluid interacting with a rotating cylinder near a solid boundary under low Reynolds number conditions. The analysis begins with the general incompressible Navier–Stokes equations and proceeds to the simplified Stokes equations, which govern the creeping flow regime relevant to this study. Special emphasis is given to the force-free configuration, where the translational motion of the cylinder emerges from hydrodynamic interactions rather than being explicitly imposed. The numerical implementation of these governing equations and associated constraints is discussed in the context of the finite element framework used throughout the simulations.

3.2.1 Navier–Stokes Equations

The Navier–Stokes equations describe the motion of an incompressible fluid. In the non-dimensional variables, it is as follows:

$$\nabla \cdot \mathbf{u} = 0, \tag{3.1}$$

$$\frac{\partial \mathbf{u}}{\partial t} + (\mathbf{u} \cdot \nabla)\,\mathbf{u} = -\nabla p + \frac{1}{Re}\nabla^2 \mathbf{u}. \tag{3.2}$$

Dimensional quantities are denoted with a tilde. We use the cylinder diameter $\tilde{D}$ as the length scale; hence, the reference velocity becomes $\tilde{U}_{\text{ref}} = \tilde{f}\,\tilde{D}$, where $\tilde{f}$ is the dimensional rotation frequency, the time scale set to $\tilde{t}_{\text{ref}} = \tilde{D}/\tilde{U}_{\text{ref}}$, and the pressure scale becomes $\tilde{P}_{\text{ref}} = \tilde{\rho}\tilde{U}_{\text{ref}}^2$. With these choices, the Reynolds number is defined as:

$$Re \;=\; \frac{\tilde{\rho}\,\tilde{U}_{\text{ref}}\,\tilde{D}}{\tilde{\mu}} \;=\; \frac{\tilde{\rho}\,\tilde{f}\,\tilde{D}^2}{\tilde{\mu}}. \tag{3.3}$$

For a spinning cylinder, the dimensional tangential speed at the surface is

$$\tilde{U}_\tau \;=\; \tilde{\Omega}\,\frac{\tilde{D}}{2} \;=\; \pi\,\tilde{f}\,\tilde{D} \qquad (\text{since } \tilde{\Omega} = 2\pi\tilde{f}) \tag{3.4}$$

so the non-dimensional no-slip condition on the cylinder surface is

$$\mathbf{u}\cdot\boldsymbol{\tau} \;=\; \frac{\tilde{U}_\tau}{\tilde{U}_{\text{ref}}} \;=\; \pi, \qquad \mathbf{u}\cdot\mathbf{n} \;=\; 0. \tag{3.5}$$

3.2.2 Stokes Equations

In this study $Re \ll 1$, so inertial effects are negligible relative to viscous stresses. Neglecting the inertial terms in (3.2) yields the steady Stokes equations in the same scaling,

$$-\nabla p + \frac{1}{Re}\nabla^2 \mathbf{u} = 0, \qquad \nabla \cdot \mathbf{u} = 0. \tag{3.6}$$

Throughout the thesis we set $D = 1$ for non-dimensionalization; thus W_x, W_z, L, and d_{wall} are reported in units of D.

3.2.3 Hydrodynamic Force Balance

In the force-free configuration, the cylinder is prescribed a rotational velocity Ω about the y-axis, while its translational velocity U in the x-direction is not imposed explicitly. Instead, the net hydrodynamic force acting on the cylinder in the x-direction is set to zero, allowing the translation to emerge from the flow field. This is implemented via the following surface integral condition:

$$\int_{S_c} \boldsymbol{\sigma} \cdot \mathbf{n}_x \, dS = 0 \tag{3.7}$$

where $\boldsymbol{\sigma}$ is the Cauchy stress tensor, S_c is the surface of the cylinder including its end caps, and $\mathbf{n}_x$ is the unit normal vector in the x-direction. In the finite-element implementation, this constraint is enforced weakly using a Lagrange multiplier, enabling the solver to determine the resulting translational velocity that satisfies the force-free condition.

Due to the imposed symmetry and geometry of the problem, the net force in the y-direction is zero, and no translation is allowed in the z-direction. Although a non-zero hydrodynamic force may still arise in the z-direction due to confinement and asymmetry, it does not contribute to motion under the assumptions of the present study.

3.3 Numerical Approach

To investigate the low-Reynolds-number hydrodynamics of a cylinder near a wall, numerical simulations were conducted using the commercially available finite element method (FEM) package COMSOL 6.2. The Creeping Flow module was employed, as viscous effects dominate the flow regime, rendering inertial contributions negligible, for the solution of the flow field. Additionally, the Global ODEs and DAEs module was utilized to ensure the hydrodynamic force balance and to implicitly solve for the cylinder. This section outlines the mesh generation strategy, solver configuration, and validation of the numerical model.

3.3.1 Mesh

During the meshing process, distinct strategies were employed for two-dimensional and three-dimensional domains due to their differing computational demands. Owing to the significantly lower computational cost of 2D simulations, finer mesh resolution and fluid discretization were adopted for the two-dimensional cases. Despite this refinement, the total number of degrees of freedom (DOFs) across all 2D simulations typically was around approximately 400,000, with the number of elements varying between 25,000 as a minimum and 1,500,000 as a maximum (for extremely small gap heights), depending on the specific geometry and aspect ratio of the domain.

For the two-dimensional geometries, the mesh was generated with respect to the cylinder radius $R = D/2$. A bounding box was defined based on the desired aspect ratio, and an additional refinement box was introduced around the cylinder to allow for local mesh refinement. Within this inner refinement region, the maximum and minimum element sizes were set to $R/10$ and $R/1000$, respectively. In the outer area, these values were set to $R/2$ and $R/200$, respectively. For both domains, the maximum element growth rate was defined as 1.1, with a curvature factor of 1.0 and a narrow region resolution of 2. To ensure accurate representation of the curved boundary of the cylinder, a quadratic Lagrange geometry shape function was used. Additionally, two boundary layers were applied along both the cylinder surface and the bottom wall, with a stretching factor of 3 and a thickness adjustment factor of 1. This meshing strategy was applied consistently across all confinement configurations and for all considered aspect ratios of the bounding box for the 2-D domains. Figure 3.3 shows a representative mesh for the 2-D domain when $d_{\text{wall}} = 8 \times 10^{-5}$, which accurately represents near-wall meshes, with 429598 DOFs.

In 3-D domains, a parametric mesh was employed to ensure geometric adaptability across varying cylinder lengths. Quadratic Lagrange elements were used to represent the curved geometry of the cylinder accurately. Along the cylinder's top, 20 element nodes were distributed. Whereas at the bottom half of the cylinder, element nodes were distributed. These nodes were later on mapped along the cylinder's surface parametrically by introducing a length-dependent function $ceil(min(30, L/(R/5)))$ to ensure decent element number for both short disks like cylinders and long cylinders. Finally, fine triangular elements at the end of the cylinder were applied, with the maximum element size being $R/10$, with the maximum element growth rate of 1.1. This mesh setup was done to ensure high resolution in regions of strong shear and pressure gradients.

For the remainder of the domain, free tetrahedral elements were used, with a growth

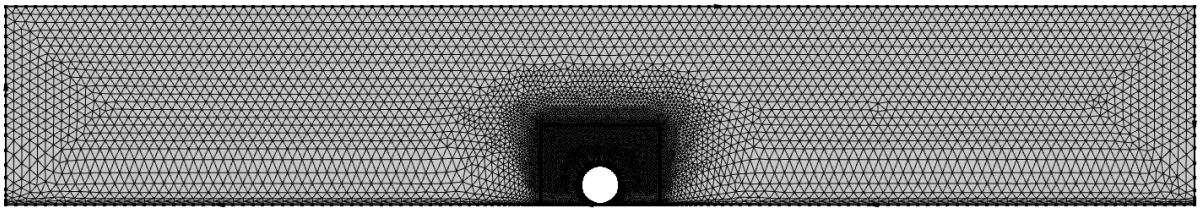

(a) Mesh of the entire computational domain

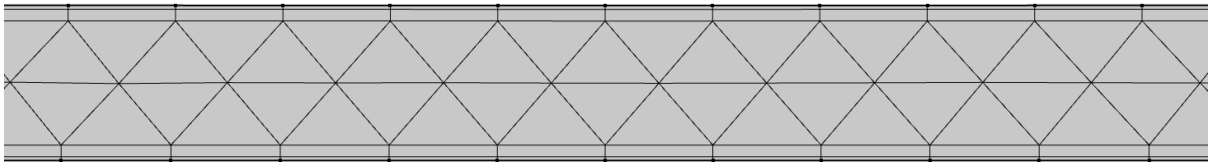

(b) Close-up view of the mesh between the bottom wall and the cylinder

Figure 3.3 Mesh configuration used in the 2-D simulations

factor of 1.2 and a curvature factor of 2 to balance element quality and computational cost. Two boundary layer meshes were introduced along the bottom wall and the sides of the cylinder with a stretching factor of one and a thickness adjustment factor of 5 to capture near-wall gradients. Overall, for this setup, the number of degrees of freedom reaches over three million in some cases, but generally remains around two million degrees of freedom. Figure 3.4 shows the full domain mesh and a close-up view near the wall-cylinder interface. For this particular case, the DOF is around 2.1 million.

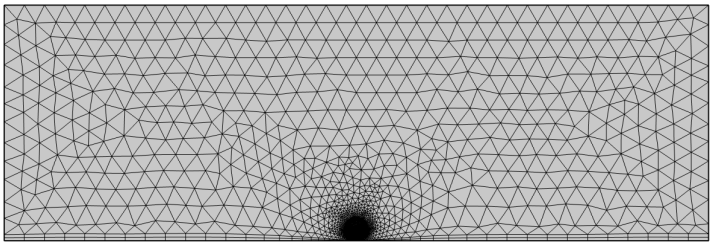

(a) Mesh of the entire computational domain viewed from the xz plane

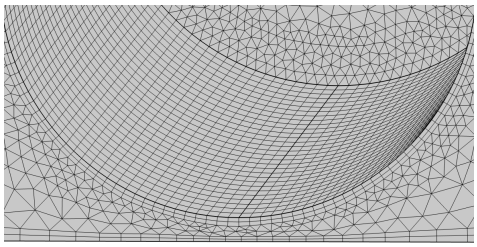

(b) Close-up view of the mesh near the bottom wall and cylinder

Figure 3.4 Mesh configuration used in the 3-D simulations

3.3.2 Solver Configuration

Simulations were performed using the finite-element method (FEM) based commercial software package COMSOL 6.2. For two-dimensional simulations, quadratic elements were employed for both the velocity and pressure fields (P2+P2 isoparametric elements).

In three-dimensional cases, a mixed formulation using P2+P1 elements (quadratic for velocity and linear for pressure) was utilized to ensure numerical stability and reduce computational cost. In both cases, quadratic elements were enforced for the geometry shape to ensure accurate isoparametric representation of the cylinder surface. Second-order Lagrange multipliers were applied as weak constraints on the cylinder boundary to impose no-slip conditions and enable accurate force calculations with quadratic convergence.

Newton's method was employed to handle the nonlinearities of the governing equations, with the system linearized at each iteration. The resulting sparse linear systems were solved using the direct MUMPS (MUltifrontal Massively Parallel sparse direct Solver), chosen for its robustness and efficiency in handling large degrees of freedom arising from fine mesh resolution. The orthonormal block size was set to 10,000,000 to accommodate the high memory demand. The maximum number of iterations is limited to 100 to ensure convergence within a reasonable computational cost. For the linear solver, the pivot threshold and scaling options were kept at their default settings. The fully coupled approach was adopted to solve all degrees of freedom simultaneously, which improves convergence for strongly coupled multiphysics problems. All simulations were conducted on a workstation equipped with an Intel i9-9000 processor and 128 GB of RAM, with 100 GB allocated to COMSOL.

3.3.3 Validation

To ensure the reliability of the numerical model, validation was carried out against results reported by Teng et al. (2022), who developed a three-dimensional lubrication theory for finite-length cylinders near rigid walls under creeping flow conditions. In particular, the hydrodynamic force acting on a translating cylinder near a rigid wall was used as the primary validation metric.

A bounding box with the dimensions $W_x = 35D$, $W_z = \frac{2}{3}W_x$ and $W_y = W_x/4$ was created and a cylinder with the length L and diameter D was placed in the geometric center of the box. The study involved a parametric investigation over the non-dimensional gap height and cylinder length. Specifically, d_{wall} was varied, across the values 0.04, 0.08, 0.2. 0.4, 0.8, 2, 4, 8, and the cylinder length was set to $L = 0.1$, 0.5, 2. No rotation was assigned to the cylinder and a unitary translational velocity $U = 1$ was given to calculate the forces for the cylinder. Figure 3.5 shows the meshing of the valida-

tion model for $d_{\text{wall}} = 0.5$ and $L = 2$, with the total of 1094972 DOFs for this particular case.

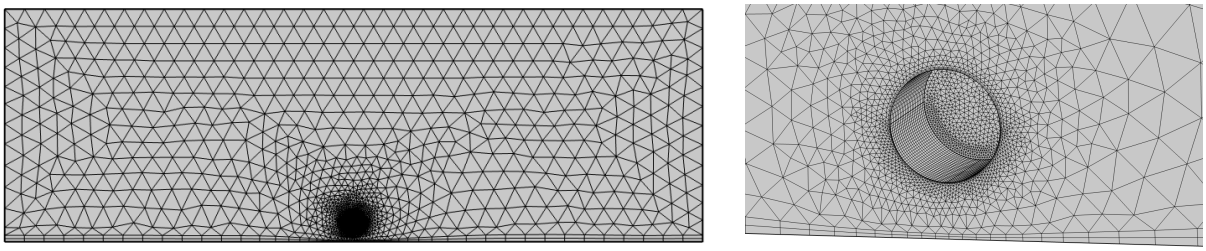

(a) Mesh of the validation model viewed from the xz plane

(b) Close-up view of the mesh near the bottom wall and cylinder for the validation model

Figure 3.5 Example mesh configuration used in the validation models

A comparison of the resulting force in the x-direction is shown in Figure 3.6, with the dashed lines representing the current model and solid lines showing the reference data from Teng et al. The relative error percentage remained below 3% across all cases, indicating strong agreement and confirming the accuracy of the implemented numerical approach.

Minor discrepancies may arise from differences in mesh density, solver tolerances, or implementation differences in the commercial package. However, these deviations were found to be negligible and do not impact the validity of the results for further parametric studies.

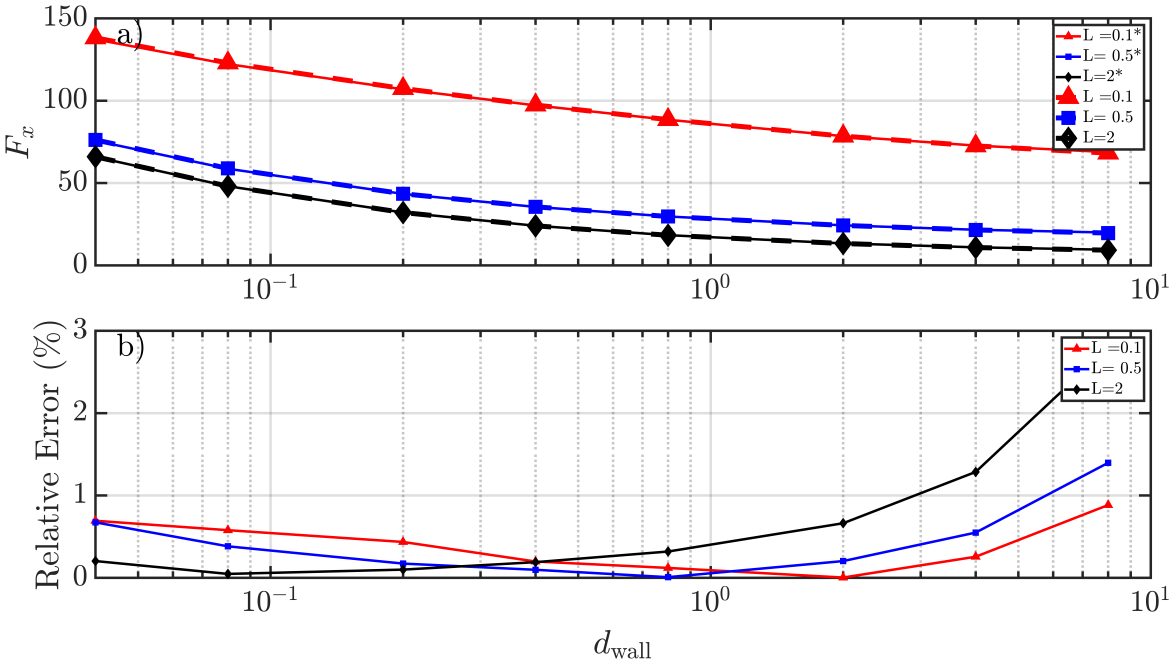

Figure 3.6 Comparison between the calculated force of the models. Figure a) The dashed lines represent the Force in the x direction of our model, and the solid lines with markers represent the results of Teng et al. (2022). b) Relative error percentage between the models.

4. RESULTS

4.1 Channel Confinement

This section presents the numerical results for the channel-type confinement, where lateral boundaries are left open (stress-free) to allow fluid exchange. This setup mimics a scenario where consistent flow from the inlet and outlet is permitted and caused by the rotation of the cylinder, enabling the examination of flow-driven pumping effects. The results are grouped by dimensionality (2D and 3D) and are discussed in terms of translational motion, hydrodynamic forces and torques, and the volumetric flow rate induced through the channel.

4.1.1 2-D Results

In the 2D simulations, the gap between the cylinder and the wall (d_{wall}) was varied across different domain aspect ratios (W_x/W_z) to analyze the proximity to the wall and how the aspect ratio of the bounding box affects the motion of the cylinder. By keeping the cylinder force-free, its translational velocity was solved implicitly as explained in Section 3.2.3.

When a rotating infinite cylinder near a wall is in an unbounded domain, no translation occurs since the cylinder experiences no force. However, in the presence of a confinement, this condition does not apply due to the flow structure becoming asymmetrical under the influence of the boundaries, and the torque and force it experiences become coupled. In Figure 4.1, the whole range of d_{wall} values for the cylinder under channel confinement

can be seen. As the $d_{\text{wall}} \to 0$, the cylinder approaches a rolling-like behavior with its velocity becoming 2π, behaving as if it is in contact with the wall. As the gap height between the cylinder and wall increases, the cylinder enters a transition region between $9 \times 10^{-6} < d_{\text{wall}} < 7 \times 10^{-5}$. The required gap height for the cylinder to start translating is affected by the aspect ratio of the bounding box, as it is highly dependent on the forces experienced by the cylinder. However, the effect of the aspect ratio shows itself much more clearly as the cylinder gets farther away from the wall, especially for $d_{\text{wall}} > 10^{-4}$

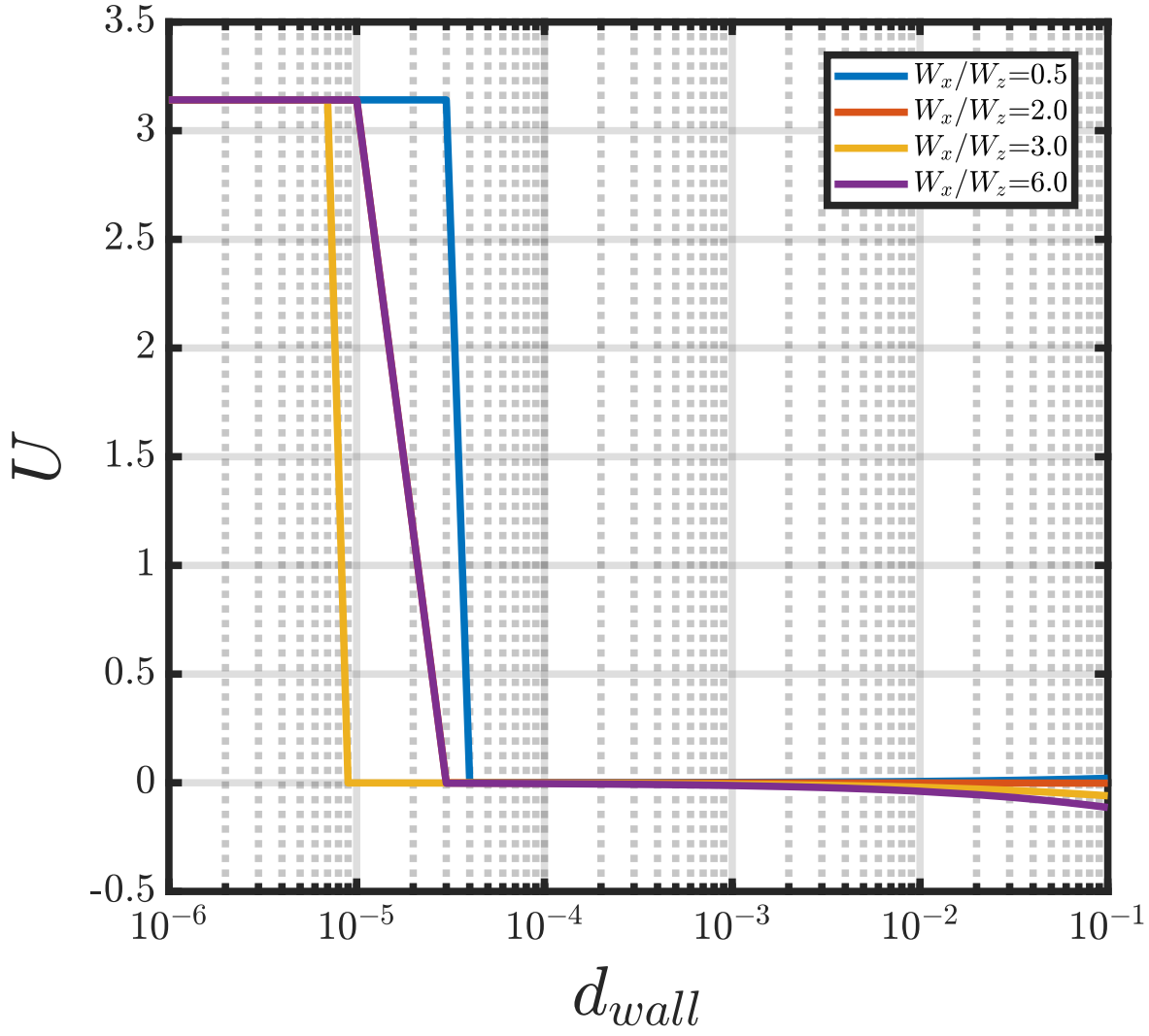

Figure 4.1 Cylinder velocities for the channel mode, shown for the full range of d_{wall} values.

Figure 4.2 shows the cylinder motion for $d_{\text{wall}} > 10^{-4}$, where the translational direction and velocity magnitude become sensitive to the domain aspect ratio. Specifically, shallow channels ($W_x/W_z \gtrsim 2$) result in negative cylinder velocity (backwards motion), while deeper channels ($W_x/W_z \lesssim 2$) lead to forward translation of the cylinder. The aspect ratio

of $W_x/W_z \lesssim 2$ becomes essential for the channel confinement as the cylinder's behavior is more enunciated as we get further away from it.

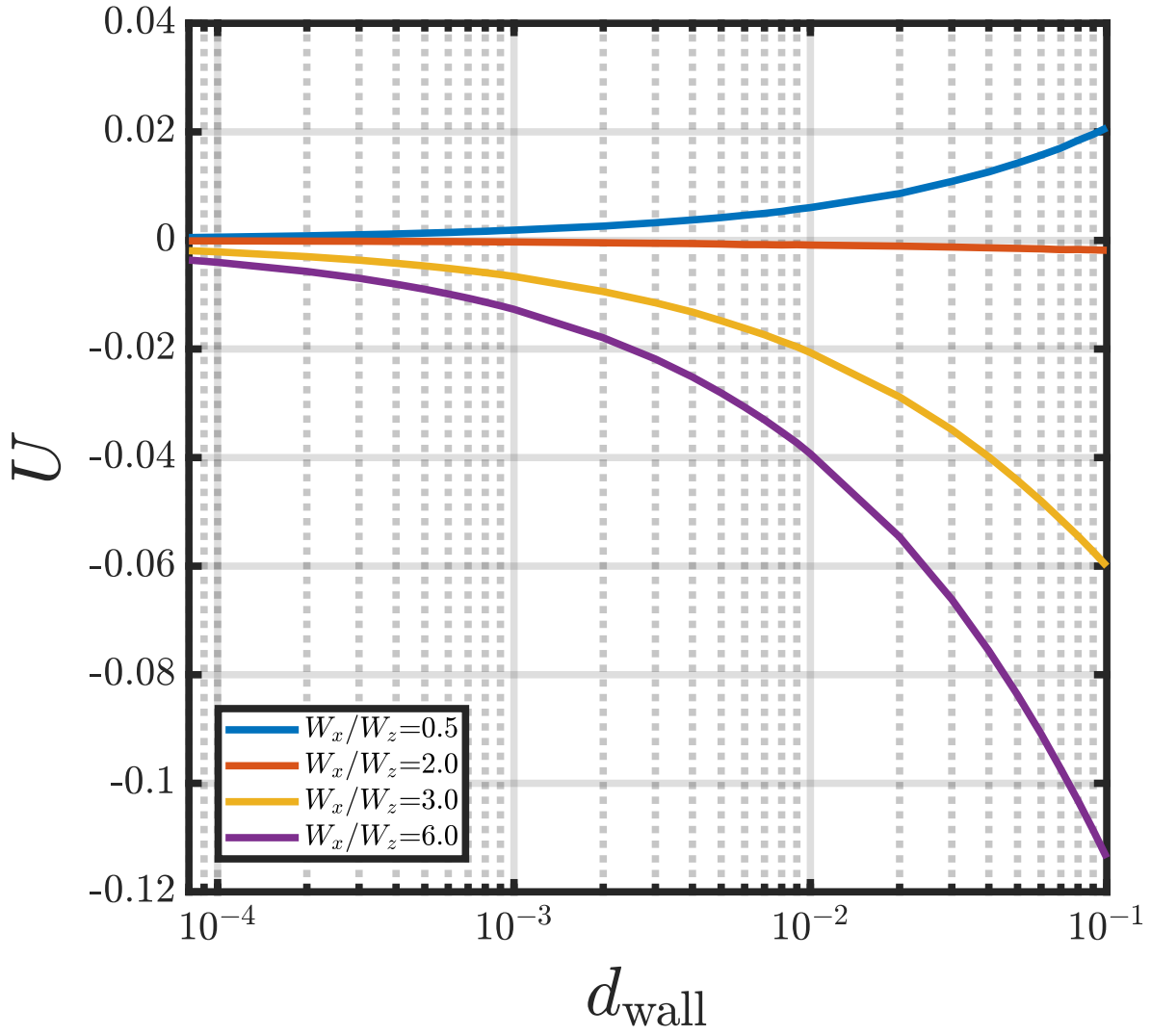

Figure 4.2 Cylinder velocities for the channel mode, shown after the transition region where the cylinder's motion starts to exhibit the confinement effect.

Figure 4.3 illustrates the volumetric flow rate at the channel inlet, calculated via integration of the velocity profile at the inlet. Unlike cylinder velocity, the flow rate shows a direct dependence on the geometric aspect ratio as $\frac{1}{W_x/W_z}$, with the slight discrepancy due to the friction experienced by the fluid as the channel gets longer in the W_x direction.

In the fixed-cylinder case, the cylinder is stationary in its place. It rotates around the y-axis, allowing examination of the hydrodynamic forces and torques that would ultimately drive translational motion under force-free conditions. The primary quantities of interest are the torque and the hydrodynamic forces acting in the x-direction. As shown in

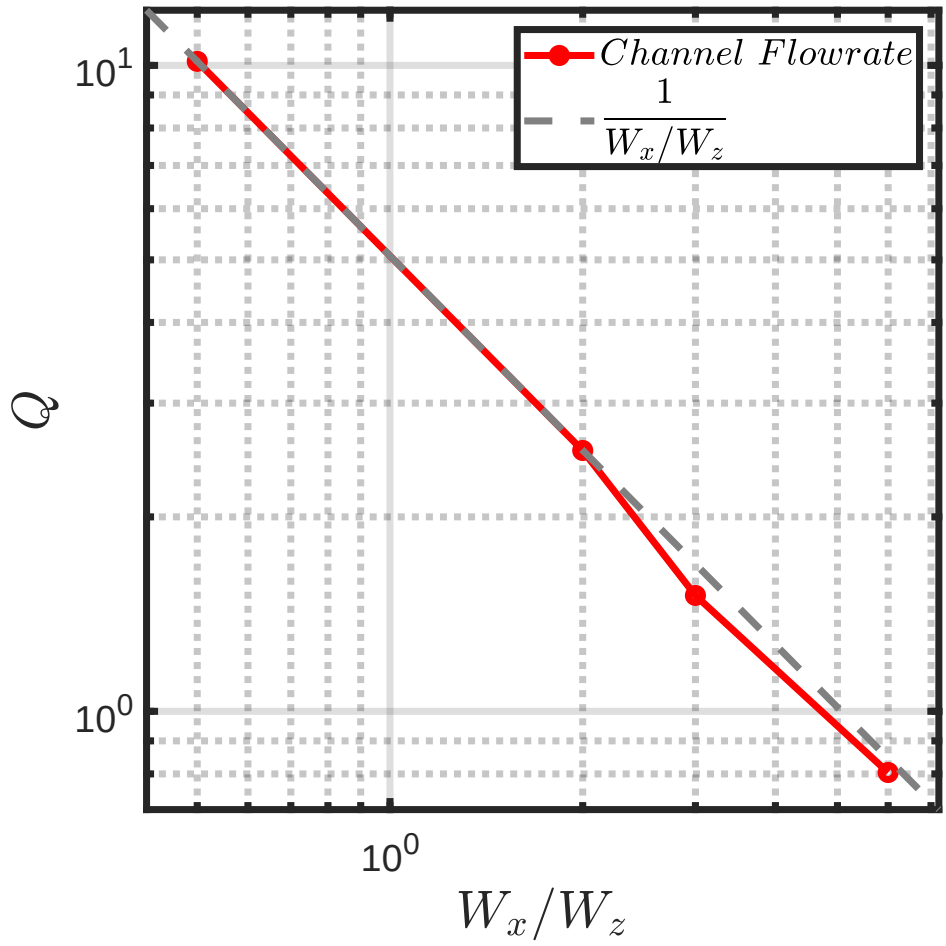

Figure 4.3 Flow rate under channel confinement, computed by integrating the velocity at the channel inlet.

Figure 4.4, the viscous torque experienced by the cylinder closely follows the analytical prediction by Jeffrey & Onishi (1981).

In contrast, the analysis of the x-direction force reveals a measurable deviation from the behavior predicted for an unbounded domain. Using Equation 2.1, the hydrodynamic force for the unbounded case is computed by substituting the translational velocity obtained from the corresponding force-free simulation, rather than assuming a unit translational velocity. As the theoretical model is derived from lubrication theory, the resulting force (represented by the dashed lines in Figure 4.4.b) corresponds to the lubrication theory prediction for an unbounded domain translating with the prescribed velocity shown in Figure 4.2. The comparison underscores the influence of confinement, particularly the proximity of the top wall, as the deviation from the theoretical prediction increases with increasing gap height. This trend identifies the range of gap heights for which the lubrication-theory formulation becomes insufficient in capturing the actual hydrodynamic

behavior under confinement.

To facilitate a comprehensive interpretation of the numerical results, the velocity fields and corresponding streamline patterns across the computational domain are presented in Figure 4.17 for a domain aspect ratio of 3, with d_{wall} values of 0.1 and 0.001. In both configurations, the rotation of the cylinder generates a localized recirculating flow between the cylinder surface and the upper boundary of the domain. This circulation is distinctly captured and delineated by the streamline patterns, making its spatial extent and orientation identifiable. Nevertheless, the velocity magnitude within this recirculating region is significantly smaller compared to the flow velocities observed along the principal inlet–outlet pathway, where the majority of the fluid transport occurs. Importantly, the volumetric flow rate is higher for smaller gap heights, due to the elevated pressure gradients generated in the confined region, which accelerate the bulk of the fluid through the main flow path.

Analysis of the pressure field further reveals that lower gap heights produce markedly elevated pressure levels in the downstream region immediately following the cylinder. This effect arises due to the increased confinement of the flow between the cylinder and the wall, which restricts fluid passage and amplifies the local pressure gradients.

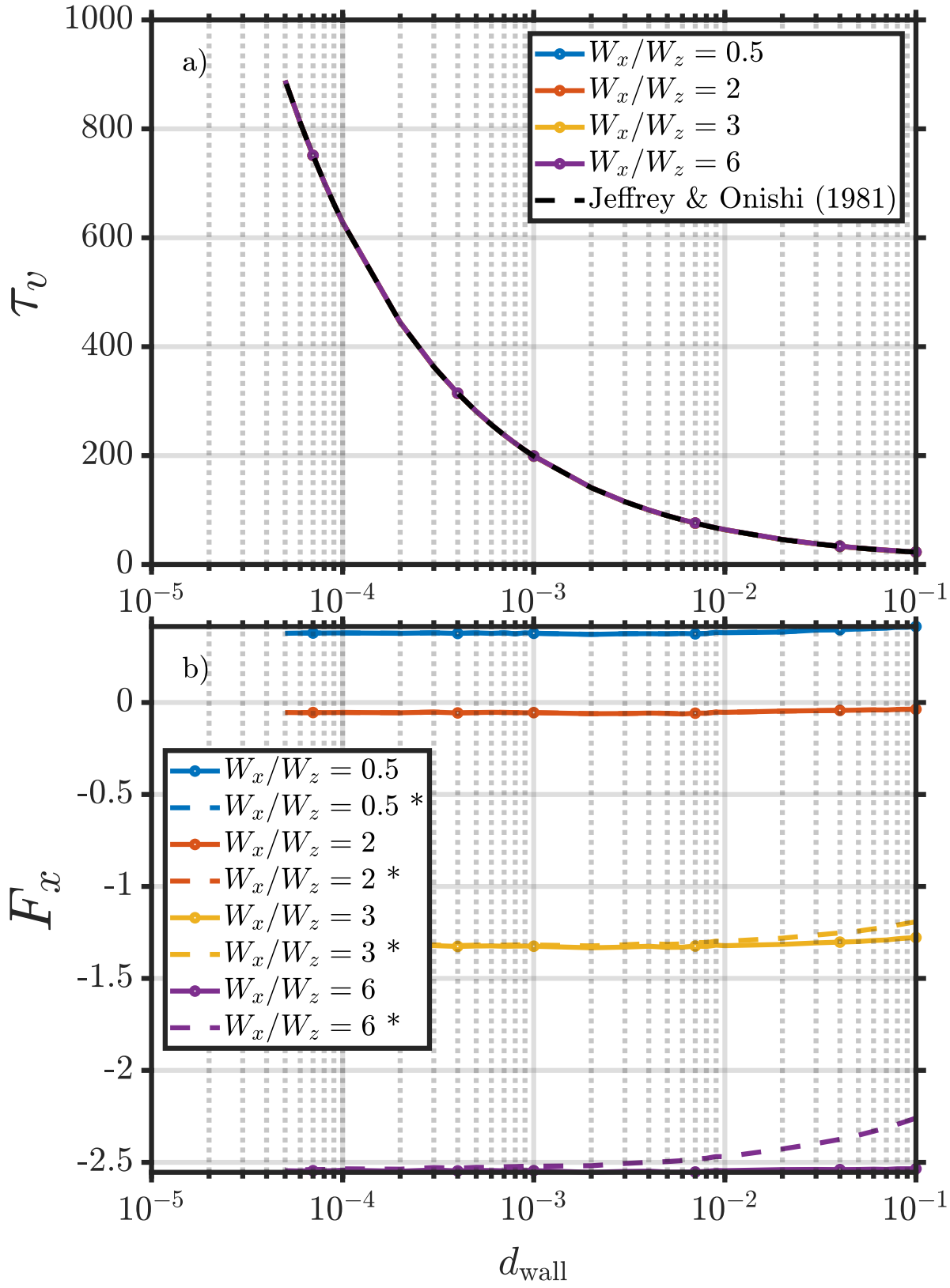

Figure 4.4 Hydrodynamic forces and torques acting on the cylinder under channel confinement. a) Viscous torque compared to Jeffery & Onishi's analytical prediction. b) Total force in x-direction, including comparison with the unbounded case (dashed lines).

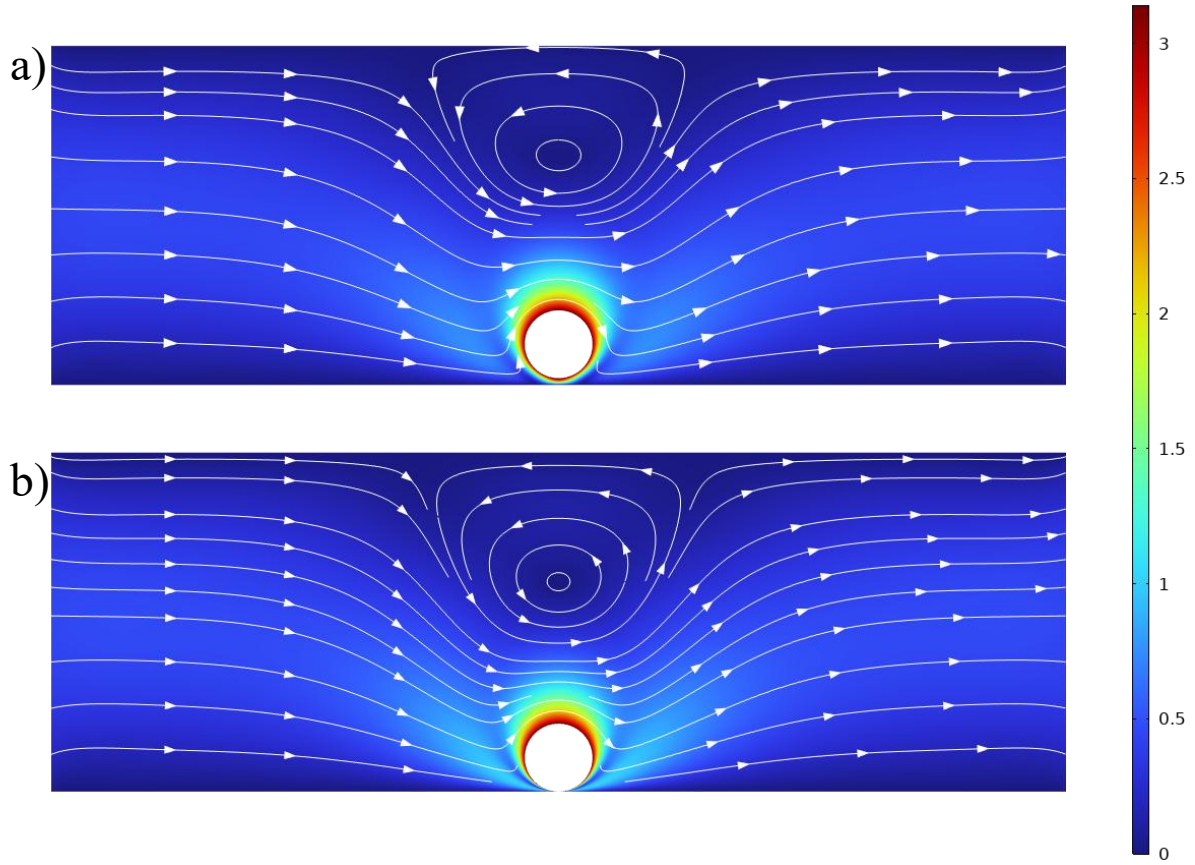

Figure 4.5 Velocity Fields and their respective streamlines under channel confinement with the $W_x/W_z = 3$ a) Results for $d_{\text{wall}} = 0.1$. b) Results for $d_{\text{wall}} = 0.001$.

4.1.2 3-D Results

The translational velocity of the cylinder in a three-dimensional channel configuration is shown in Figure 4.6. For short, disk-like cylinders, the influence of the back wall on the surrounding flow remains minimal. As a result, the cylinder's velocity remains relatively constant regardless of the domain width in the y-direction (W_y). However, as the cylinder length L increases, the proximity of the cylinder ends to the back wall begins to affect the flow field significantly. The reduced clearance between the cylinder ends and the lateral wall constrains the flow, thereby altering the hydrodynamic environment and influencing the cylinder's motion. This effect becomes evident through the onset of slipping behavior, particularly for longer cylinders, even if the resulting translational velocity remains relatively small in magnitude.

To rationalize this behavior, the hydrodynamic force distribution is examined under fixed-cylinder conditions. As shown in Figure 4.7, the total force acting on the cylinder, normalized by its length, decreases with increasing cylinder length, a trend consistent with the observed reduction in velocity magnitude. For short cylinders, the influence of the back wall remains approximately constant across all values of W_y, whereas for longer cylinders the effect of domain length becomes more pronounced.

When the total force is decomposed into contributions from the cylinder caps and the lateral sides (all resolved in the x-direction), the caps are found to account for roughly 30% of the total force in the case of short cylinders. However, as the cylinder length increases, the relative contribution of the caps becomes highly sensitive to the domain length. For moderate-length cylinders ($L = 3$), short domains yield cap contributions as high as 47% of the total force, whereas in long domains this value decreases to approximately 34%. In contrast, for long cylinders ($L = 6$), the trend reverses: in short domains, the caps contribute only about 5%, while in long domains their contribution rises dramatically to 91%. At this point, the dominance of the cap forces alters the direction of motion, producing forward translation instead of the backward slip observed for long cylinders in short domains.

Although the total force decreases with cylinder length, these results demonstrate that the cap contribution cannot be neglected. On the contrary, the strong dependence of the cap forces on both cylinder length and domain confinement highlights their central role in determining the net hydrodynamic response of the system.

Finally, the lateral forces acting on the cylinder are examined with respect to their physical origin. Under Stokes flow conditions, these forces can be decomposed into two distinct

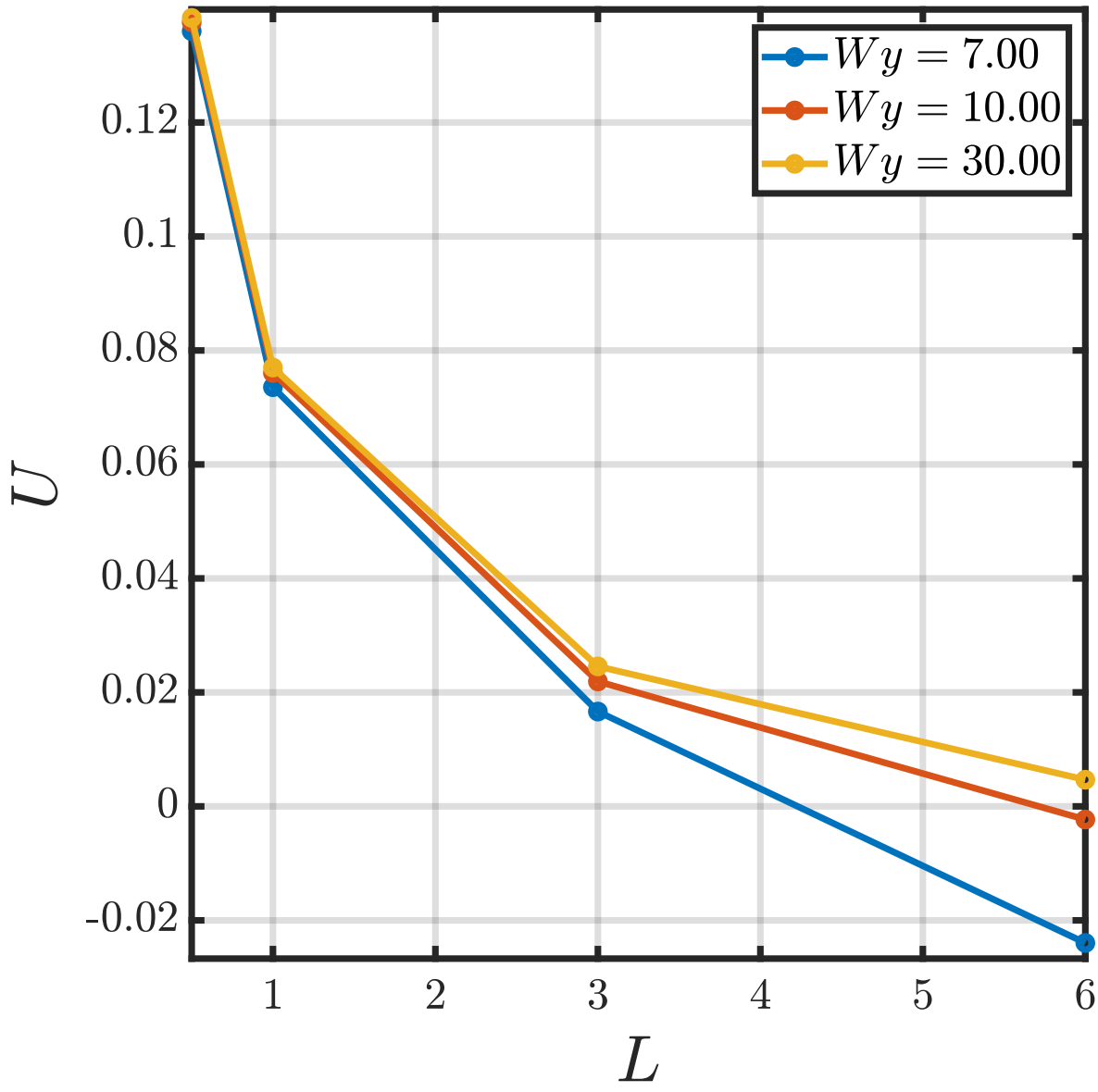

Figure 4.6 Translational velocity of the cylinder in the x-direction under channel-type confinement for various domain widths W_y.

contributions: pressure-driven forces and shear-driven forces. As anticipated, the rotation of the cylinder gives rise to pressure and shear components that act in opposite directions, with both increasing in magnitude as the cylinder length is extended. The relative rate of increase, however, is influenced by the domain length and ultimately determines the net hydrodynamic behaviour of the cylinder.

For shorter cylinders, the domain length exerts little influence on the relative balance of forces, and the shear-driven contribution dominates over the pressure-driven component. As a result, cylinders of small length exhibit comparable dynamical behavior irrespec-

tive of their exact size. By contrast, as the cylinder length increases and the domain length begins to affect the flow structure significantly, the relative growth of the two force components diverges. For instance, in the short-domain configuration ($W_y = 7$), the shear-driven forces increase by approximately 8.17%, whereas the pressure-driven forces exhibit a much larger increase of about 20%. In longer domains, however, this trend is reversed: the increase in pressure-driven forces decreases to around 19%, while the shear-driven forces rise to 8.78%. These variations underscore the sensitivity of the force balance to both cylinder length and domain confinement, highlighting their role as decisive factors in determining the resulting cylinder motion

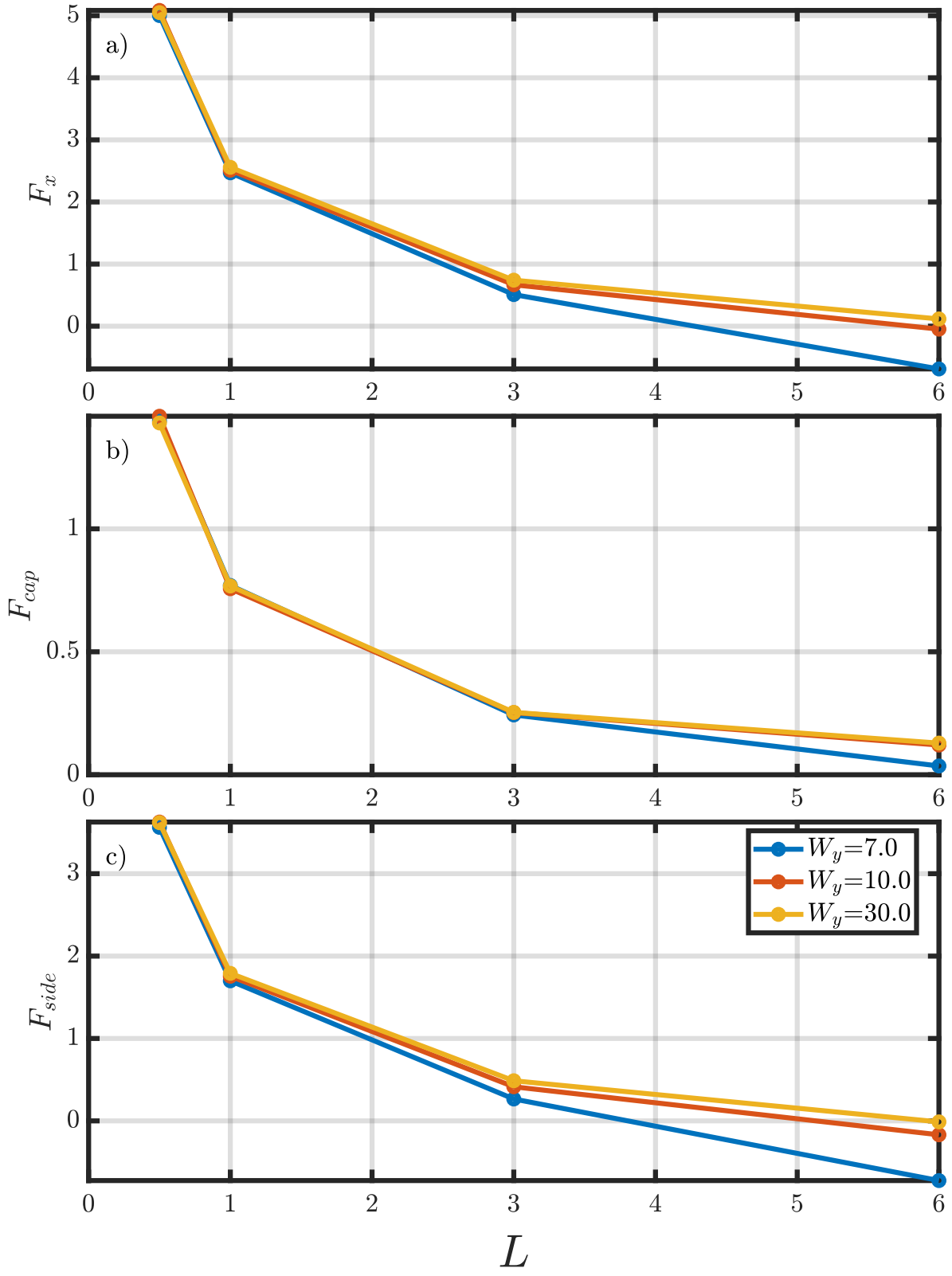

Figure 4.7 Hydrodynamic forces and torques acting on a finite-length cylinder with varying W_y under channel-type confinement. a) Total force in the x-direction; b) Force at the cylinder ends; c) Force on the cylinder sides;

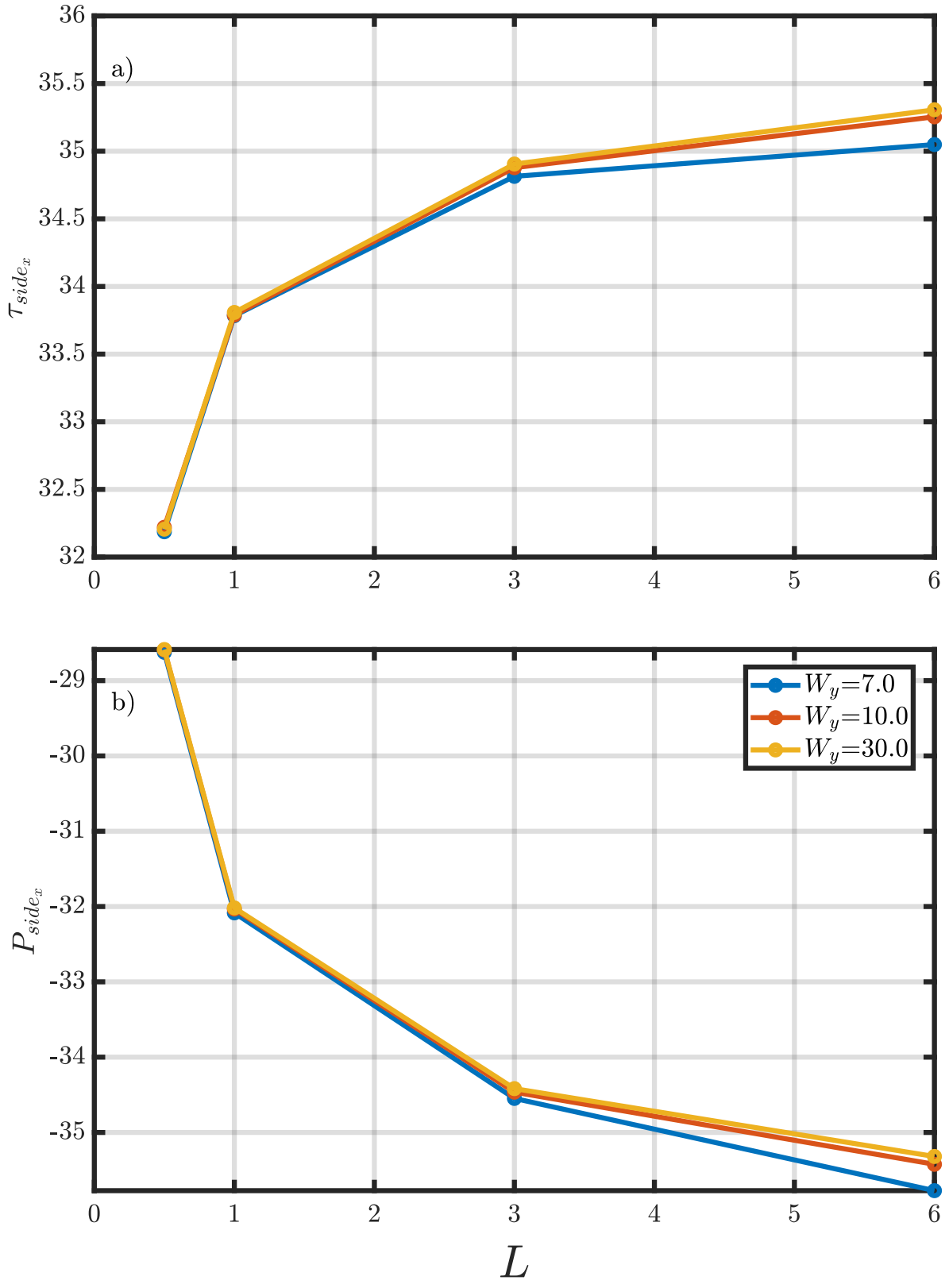

Figure 4.8 Hydrodynamic forces and torques acting on a finite-length cylinder's side with varying W_y under channel-type confinement. a) Shear-induced torque on the sides; b) Pressure force on the sides;

4.2 Closed Tank Confinement

The closed tank confinement represents the most constrained flow environment considered in this study, wherein all boundaries of the domain are closed and no-slip walls. This setup eliminates any flow paths, resulting in fully entrapped flow. The objective of this configuration is to investigate how the cylinder behaves under complete hydrodynamic confinement, especially in the presence of recirculating flows generated by the cylinder's rotation.

Significant differences are observed between the two and three-dimensional simulations in terms of cylinder motion. In the two-dimensional cases, the cylinder consistently exhibits a backward slipping motion regardless of the aspect ratio of the computational domain. As shown in Figure 4.9, the influence of confinement manifests in the magnitude of this slipping motion, which eventually saturates as the aspect ratio W_x/W_z increases. This indicates that beyond a certain increase in the domain aspect ratio, it has a negligible influence on the cylinder's translational velocity.

In contrast, the three-dimensional simulations reveal more nuanced behavior. Backward slipping motion is only observed for sufficiently elongated cylinders (i.e., high L) and when the axial domain width W_y remains small to moderate. When W_y is large, the increased clearance between the cylinder ends and the back wall allows more fluid motion, thereby reducing the forces responsible for translation. As a result, slipping is suppressed in wider domains, underscoring the critical role of axial confinement in three-dimensional environments (see Figure 4.12).

4.2.1 2-D Results

The translational velocity of the cylinder is obtained by imposing a force-free condition in the x-direction, as defined in Equation 3.7. The influence of complete confinement on the resulting motion is presented in Figure 4.9. In contrast to the forward motion observed in channel-type configurations (Figure 4.2), the cylinder consistently moves in the backward direction when placed in a confined tank. This reversal in direction highlights the strong impact of global recirculation and flow obstruction within the domain. Moreover, the cylinder's velocity asymptotically approaches a constant value beyond an aspect ratio of

$W_x/W_z \approx 3$, demonstrating that the vertical extent of the domain with respect to its width ceases to influence the hydrodynamic interactions.

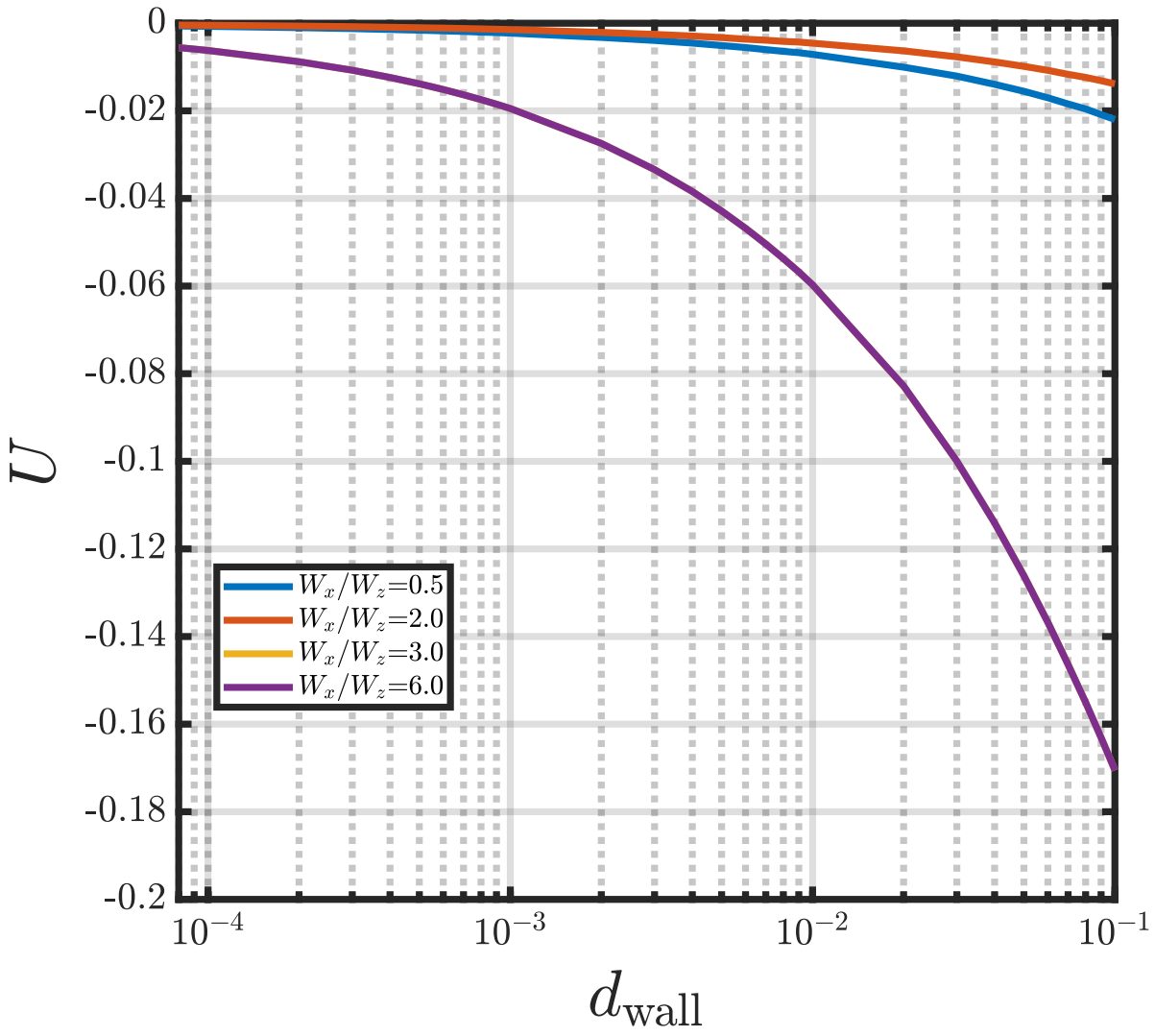

Figure 4.9 Translational velocity of the cylinder under closed tank confinement in 2-D, shown after the transition region where confinement-induced effects dominate the motion.

To analyze the forces responsible for the slipping behavior, the cylinder is held fixed, allowing direct computation of the hydrodynamic torque and force. As shown in Figure 4.10, the viscous torque acting on the cylinder aligns well with the analytical expression provided by Jeffrey & Onishi (1981), remaining unaffected by domain confinement. However, the total force in the x-direction reveals a clear dependence on the aspect ratio. Notably, the force magnitudes for $W_x/W_z = 3$ and $W_x/W_z = 6$ are nearly identical, which is consistent with the observed velocity saturation under the force-free condition.

Furthermore, comparison of the forces experienced by the cylinder with the theoretical force calculated using Equation 2.1 for unbounded domains reveals a significant deviation.

This discrepancy arises due to confinement effects, which alter the macro flow structure within the domain.

To develop a more comprehensive understanding of how complete confinement influences the slip behaviour of the cylinder, the streamline patterns and velocity fields across the entire computational domain are examined for an aspect ratio of 3 with d_{wall} values of 0.001 and 0.1. As illustrated in Figure 4.9, both configurations exhibit slip; however, the slip velocities differ markedly between the two cases. Owing to the fully confined nature of the domain, the flow exhibits a continuous recirculation zone that extends throughout the bulk of the domain. The intensity and spatial extent of this recirculating flow directly influence the hydrodynamic forces acting on the cylinder, thereby governing the magnitude of slip.

The influence of gap height on the global flow structure becomes particularly evident when comparing the relative extents of the recirculation regions. For larger d_{wall}, the primary recirculation zone occupies a greater proportion of the domain, extending further into the main flow path relative to configurations with smaller gap heights. In addition to the dominant central recirculation, secondary vortical structures are observed in the corners of the domain; the size of these corner recirculations decreases progressively as the gap height increases, indicating a systematic reorganisation of the overall flow topology. Examination of the near-cylinder velocity field shows that, for smaller gap heights, the fluid near the cylinder attains higher velocities than in cases with larger gap heights.

Moreover, a detailed comparison of shear-driven and pressure-driven contributions to the hydrodynamic loading provides a more refined understanding of the mechanisms underlying slip behaviour. For larger gap heights, the upper surface of the cylinder is subjected to a pronounced shear-driven force component, whereas in the smaller gap heights this contribution is negligible. This shift in the relative dominance of shear and pressure forces plays a key role in determining the observed differences in slip dynamics between the two gap-height conditions.

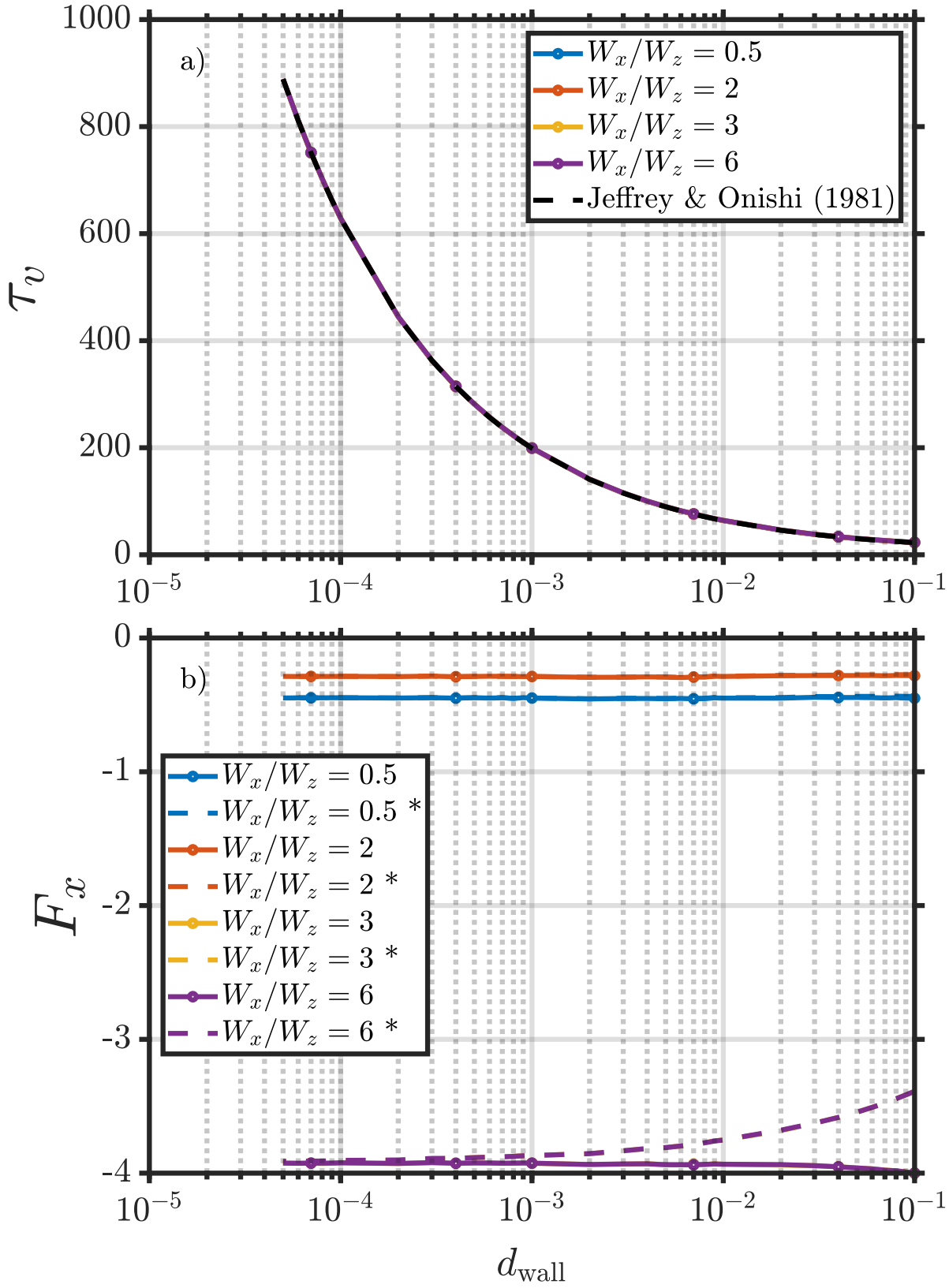

Figure 4.10 Hydrodynamic forces and torques acting on the cylinder under closed tank confinement. a) Viscous torque compared with the analytical solution of Jeffrey & Onishi (1981). b) Total hydrodynamic force in the x-direction. The superposition of curves for $W_x/W_z = 3$ and $W_x/W_z = 6$ illustrates the asymptotic behavior of the confined force response.

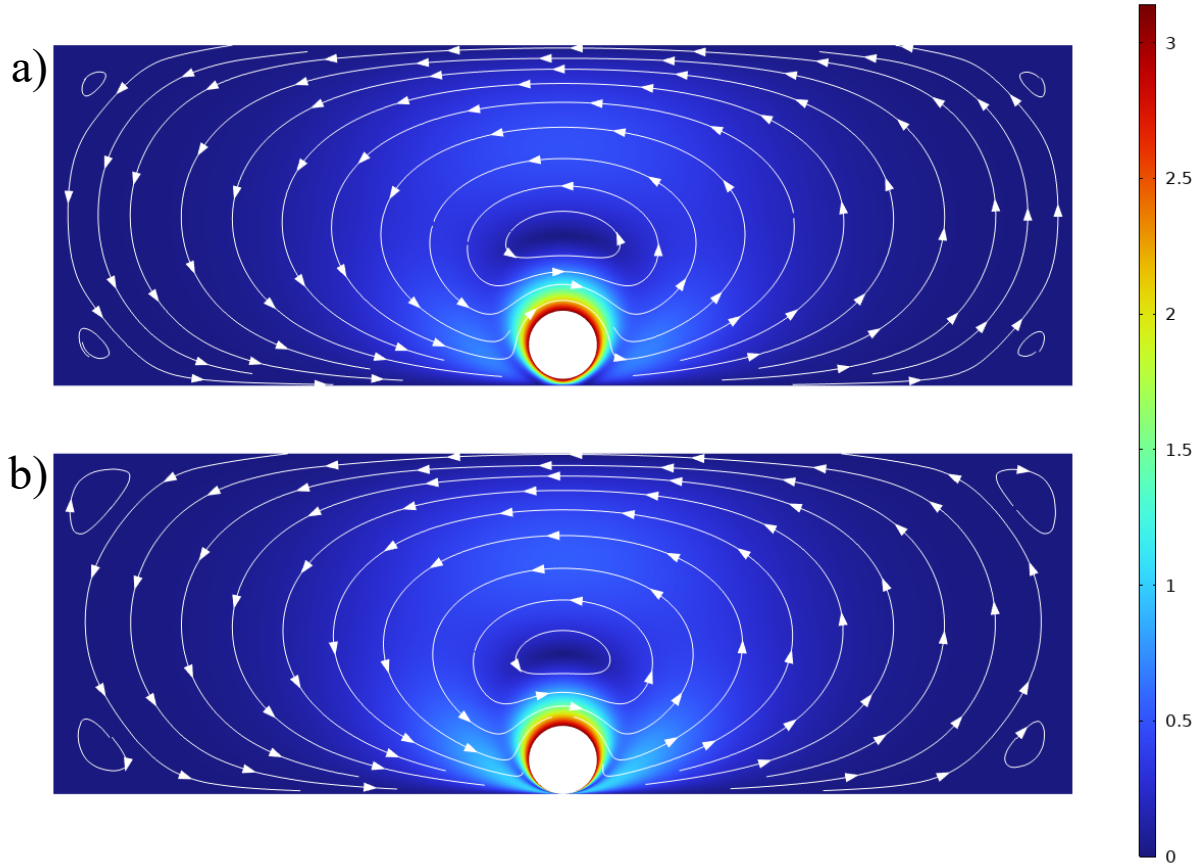

Figure 4.11 Velocity Fields and their respective streamlines under closed tank confinement with the $W_x/W_z = 3$ a) Results for $d_{\text{wall}} = 0.1$. b) Results for $d_{\text{wall}} = 0.001$.

4.2.2 3-D Results

Three-dimensional simulations under force-free boundary conditions were conducted to explore the influence of both cylinder length L and domain width W_y on the resulting translation. As shown in Figure 4.12, backward motion persists only when the cylinder is sufficiently long and the domain is narrow in the y-direction. This trend reflects the critical role of lateral confinement in shaping the flow field. Specifically, for shorter cylinders or wider domains, the flow can bypass the cylinder ends with minimal resistance, reducing the net hydrodynamic force and thereby suppressing translation.

Beyond the cylinder's velocity, the influence of confinement can also be assessed through the lateral forces acting on the cylinder. The effect of confinement on these forces becomes apparent beginning with the moderate cylinder length of $L = 3$, irrespective of the domain length W_y, with the notable exception of the cap contributions. The forces originating from the cylinder caps are only significantly affected when the back wall is sufficiently close to the cylinder ends to alter the flow structure. Consequently, the relative contribution of the caps varies strongly with both cylinder length and domain confinement.

For short cylinders, the cap contribution remains approximately constant at 27–29% of the total force. However, as the contribution from the side surfaces decreases, the cap contribution rises to about 68% in the short-domain configuration and 34% in the long-domain configuration. With increasing cylinder length, the side forces not only change in magnitude but also reverse direction, thereby diminishing the relative contribution of the caps. For example, at $L = 6$, the cap forces account for only 4% of the total in the short-domain case, whereas in the long-domain case this value increases substantially to 61%.

These results underscore that the relative importance of cap versus side forces is strongly modulated by both cylinder length and domain confinement. As the side forces evolve in magnitude and direction with increasing length, a detailed examination of the dominant contributions becomes essential for accurately characterizing the overall hydrodynamic behaviour.

The influence of axial confinement is further demonstrated by analyzing the distribution of shear and pressure-induced forces acting on the cylinder. As illustrated in Figure 4.14, these forces change with the domain width W_y and cylinder length L. Notably, the combination of shear forces and pressure-driven contributions on the cylinder's side surfaces can become sufficiently negative to induce net translation in the x-direction. This mechanism is particularly relevant for longer cylinders, where confinement effects inten-

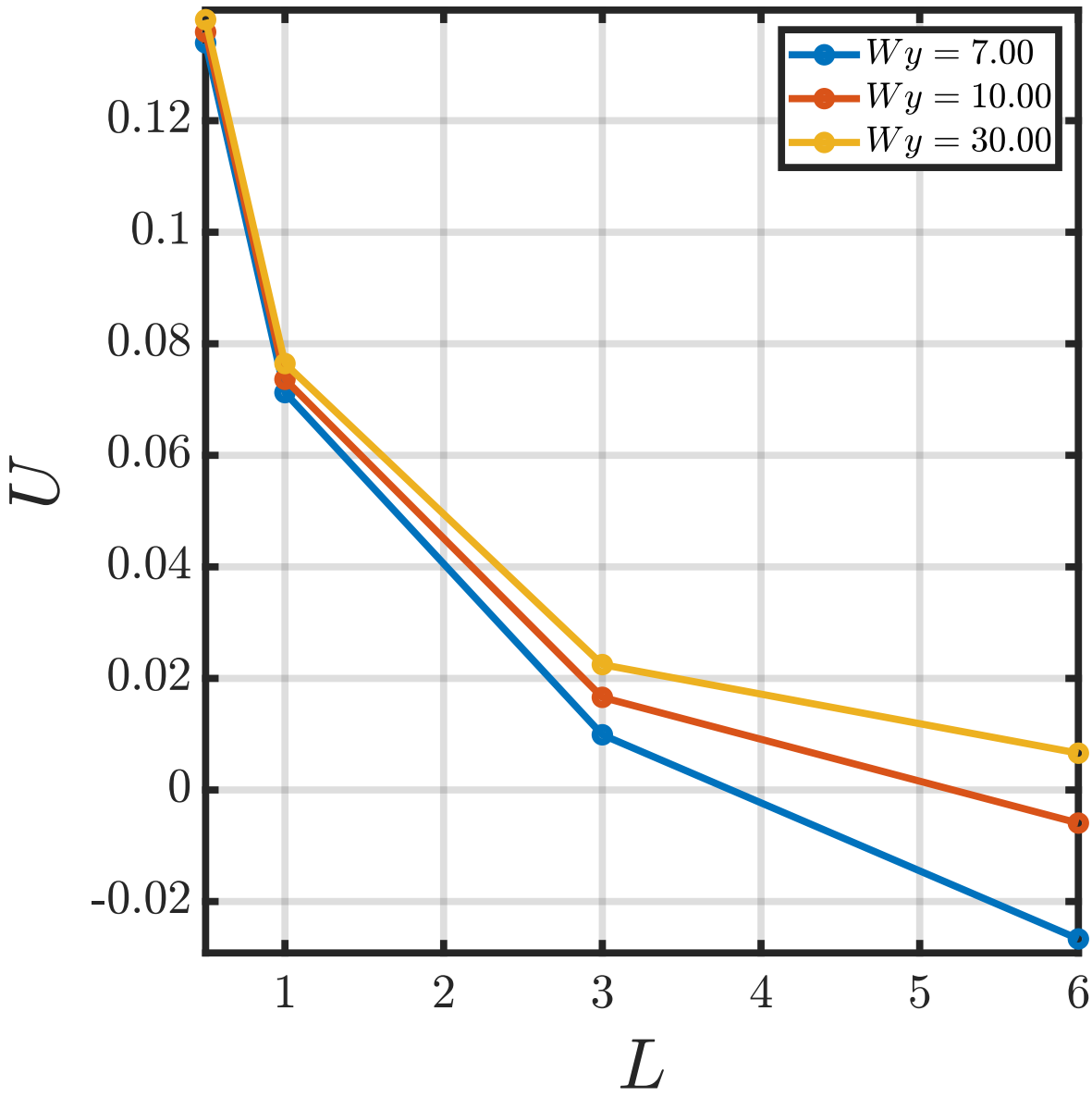

Figure 4.12 Translational velocity of the cylinder in the x-direction under closed tank confinement for various W_y values. Backward slipping is observed for long cylinders in narrow domains.

sify due to limited axial clearance. Figure 4.13.c highlights this behavior by showing the summed contributions of torque and pressure forces on the cylinder's surfaces, revealing the hydrodynamic conditions under which slipping motion is initiated.

For shorter cylinders, the shearing and pressure-driven forces on the sides of the cylinder have a much lower magnitude as opposed to the longer cylinder cases, in contrast to the forces at the caps of the cylinder, which are higher. Even though the lower magnitude of the dominating forces over the cylinder, it experiences a forward translation with higher

velocity because, the pressure-driven forces which are the opposing force that causes cylinder to exhibit the slipping motion, are not enough to dominate both the forces at the cylinders ends and the shearing forces on its sides.

In narrow domains ($W_y \lesssim 10$) with long cylinders $L = 6$, pressure-driven forces dominate due to strong confinement effects on the macro flow within the domain. In contrast, in wider domains, shear forces gain relative prominence. The slipping motion arises in cases where pressure forces surpass the resisting shear forces on the cylinder's sides, providing the net driving force required for translation. This trend underscores the importance of flow confinement in both transverse and axial directions for enabling motion.

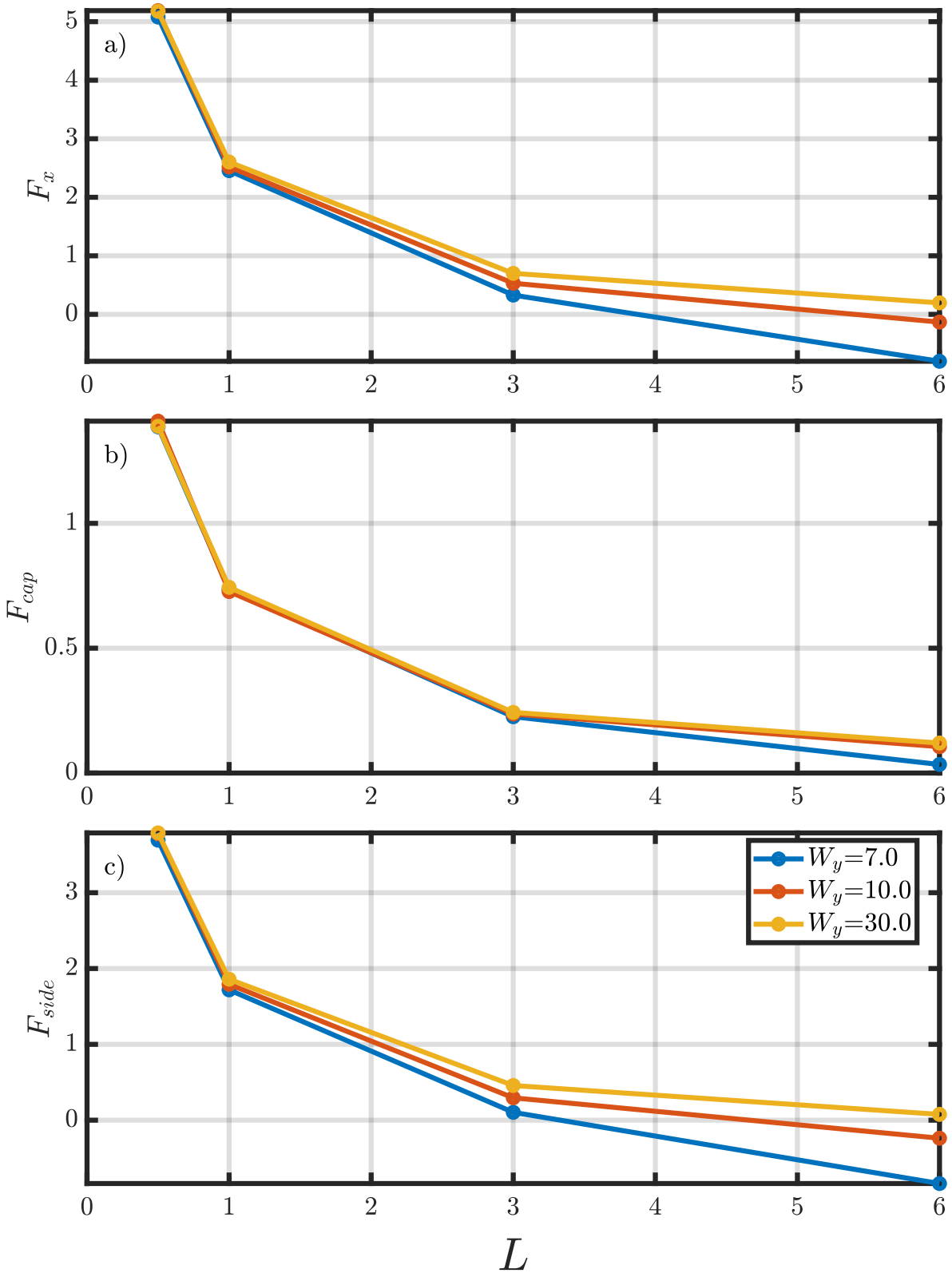

Figure 4.13 Hydrodynamic forces and torques on a finite-length cylinder under closed tank confinement with varying W_y. a) Total force in the x-direction; b) Force on cylinder ends; c) Force on cylinder sides;

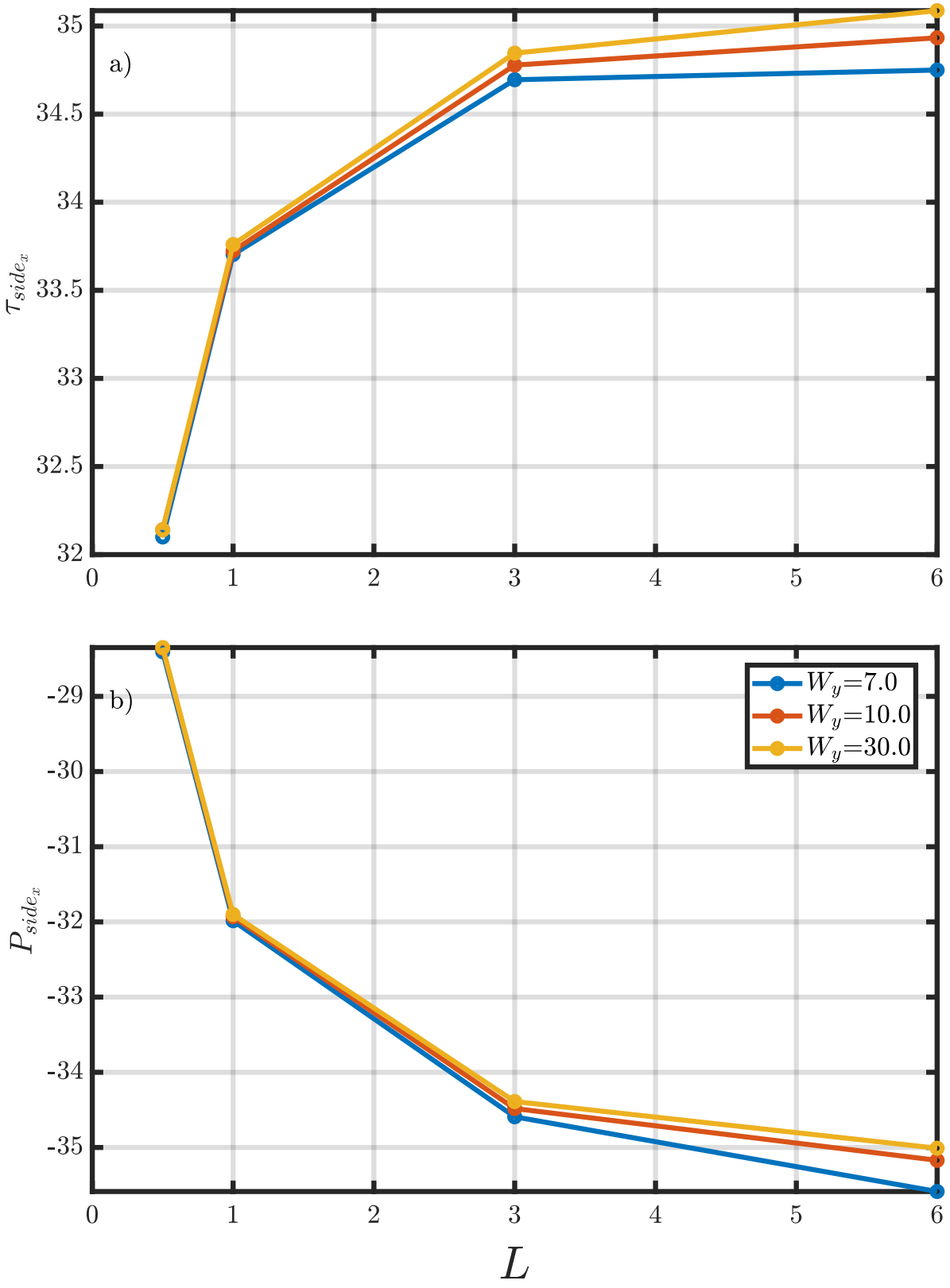

Figure 4.14 Hydrodynamic forces and torques acting on a finite-length cylinder's side with varying W_y under channel-type confinement. a) Shear-induced torque on the sides; b) Pressure force on the sides;

4.3 Open Tank Confinement

The open tank configuration investigates the hydrodynamic behavior of a cylinder in a partially confined domain, where the top boundary is open while all other boundaries are sealed. This arrangement, resembling an aquarium, allows fluid to enter and escape through the top, thereby altering the global flow topology compared to the fully enclosed configuration discussed in Section 4.2. The aim is to evaluate how partial confinement modifies the forces acting on the cylinder and its resulting motion.

In the 2-D cases, the aspect ratio of the domain strongly influences the direction of motion. As the tank becomes deeper (i.e., larger W_x/W_z), the cylinder transitions from backward slipping to forward translating motion. In contrast, the 3-D simulations highlight the influence of axial confinement; slipping motion is only observed for sufficiently long cylinders in relatively narrow domains. For example, while a 2-D cylinder may move forward at $W_x/W_z = 3$, its 3-D counterpart will only slip if both the cylinder is long and the domain is sufficiently narrow, a condition that closely resembles its 2-D counterpart.

The results from the force analysis reinforce this observation. In 2-D, the magnitude and direction of the hydrodynamic force along the x-axis are directly linked to the presence or absence of the top wall. In 3-D, the relative contributions of shear and pressure forces on the sides of the cylinder become dominant factors governing the net force in x direction and, consequently, the translational behavior.

4.3.1 2-D Results

The translational velocity of the cylinder is computed under force-free conditions by enforcing a zero net hydrodynamic force in the x direction. This setup allows investigation of the macro flow interactions and their influence on the direction and magnitude of the cylinder's motion.

As illustrated in Figure 4.15, as the gap increases, confinement effects become more pronounced. The results reveal a critical dependence on the domain aspect ratio W_x/W_z. In shallower domains, the cylinder moves forward, while in deeper domains, the effect of the macro flow generates backward slipping motion. This transition in motion direction

demonstrates the sensitivity of the cylinder to global flow structures imposed by the confinement geometry.

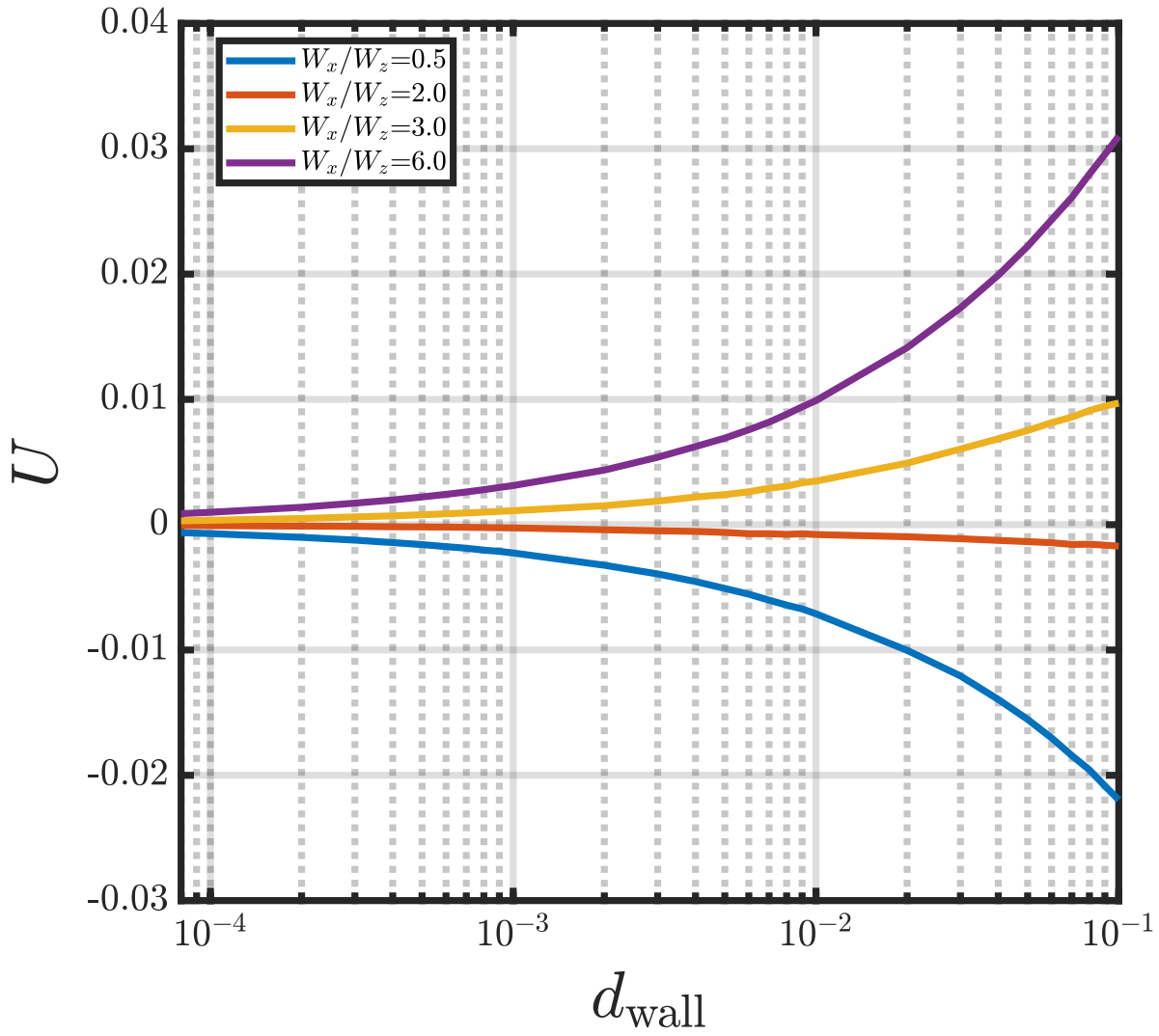

Figure 4.15 Translational velocity of the cylinder in the x-direction under open tank confinement in 2-D. Results are shown beyond the initial transition region to capture confinement-dominated behavior.

The fixed-cylinder simulations enable evaluation of the hydrodynamic forces and torques acting on the cylinder surface. Figure 4.16 presents the results for viscous torque and net force in the x-direction. The viscous torque (Figure 4.16.a) is consistent with the analytical predictions of Jeffrey & Onishi (1981) and prior confinement configurations. However, the net force in the x-direction shows a clear sensitivity to tank depth. At lower aspect ratios, the force is positive (forward motion), while at higher aspect ratios, it becomes negative, driving backward slipping motion.

Interestingly, the agreement between the numerically computed forces and the theoretical

predictions from unbounded domain analysis is more nuanced in the open tank configuration. This suggests that the influence of the open top boundary is qualitatively different from that of lateral walls, showcasing the importance of the top boundary and highlighting that in its absence, the force experienced by the cylinder is much closer to that of the unbounded cylinder when compared to the other confinement configurations. The effect of this can also be seen in the velocity of the cylinder, as its magnitude both for forward translation and backward slipping is much lower.

For the further understanding of the macroflow within the domain, analysis of the streamlines and velocity magnitudes of the domain is performed for the aspect ratio of 3 and d_{wall} values of 0.1 and 0.001, respectively. Unlike the cases before, no dominating recirculation zones appear in the open tank confinement due to the absence of the top wall; however, small secondary recirculations appear at the bottom corners of the domain. The size of these zones is dependent on the gap height, as the gap height increases, the zones become larger, but their effect on the macro flow remains minimal.

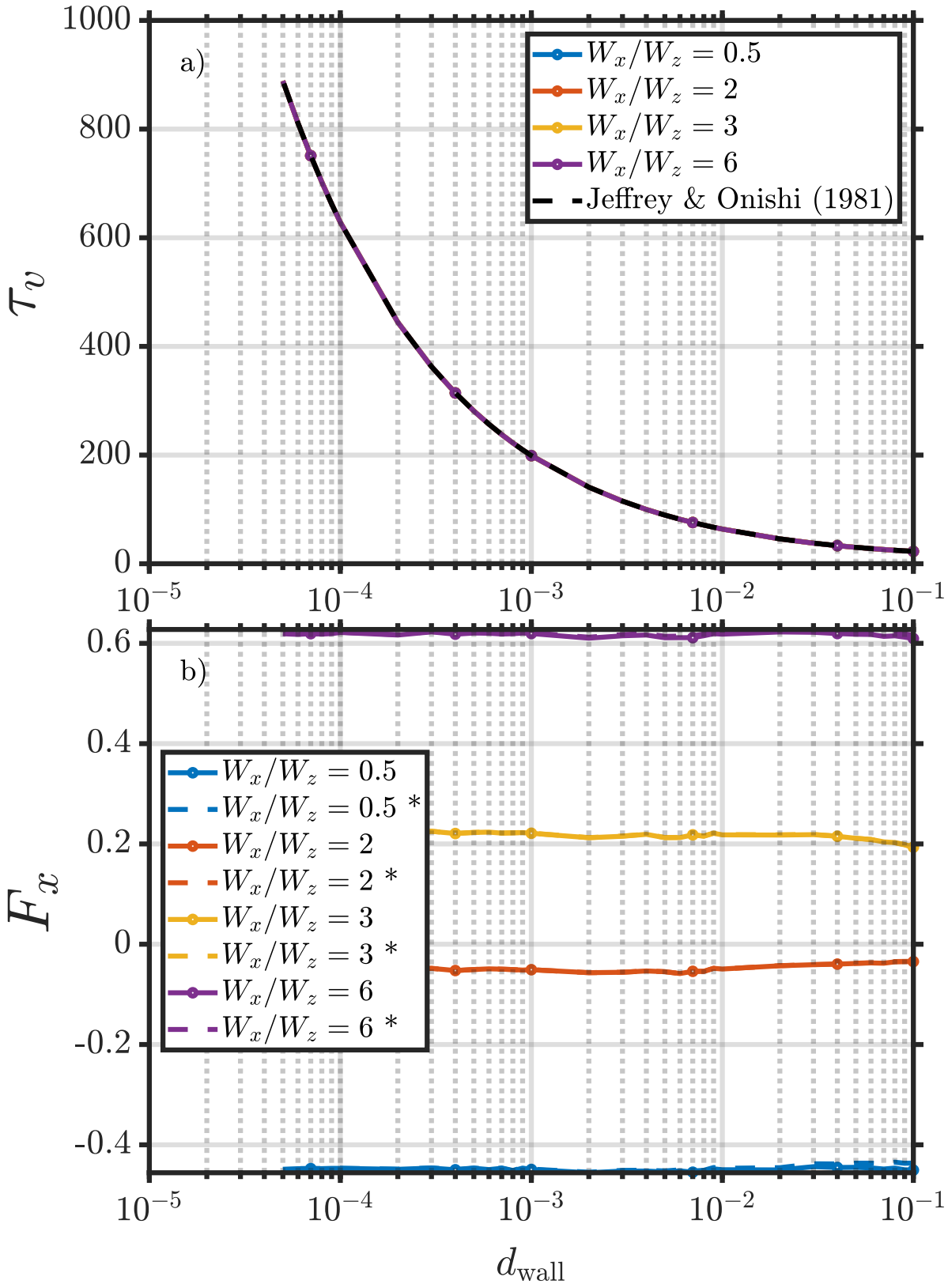

Figure 4.16 Hydrodynamic forces and torques acting on the cylinder under open tank confinement. a) Viscous torque compared to the analytical model of Jeffrey & Onishi (1981); b) Viscous force in the x-direction; c) Total hydrodynamic force. Force direction changes with domain aspect ratio, indicating confinement-dependent motion.

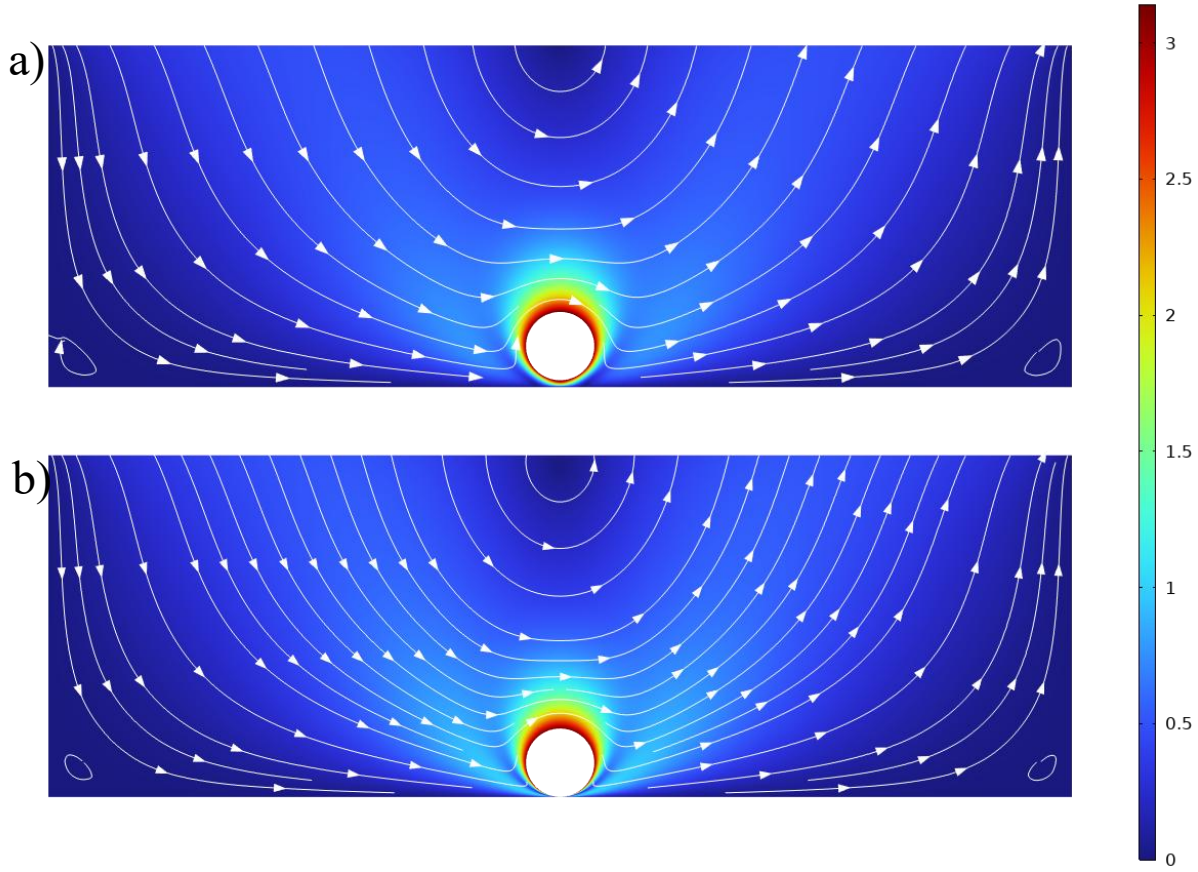

Figure 4.17 Velocity Fields and their respective streamlines under open tank confinement with the $W_x/W_z = 3$ a) Results for $d_{\text{wall}} = 0.1$. b) Results for $d_{\text{wall}} = 0.001$.

4.3.2 3-D Results

In 3-D simulations, the cylinder's translational velocity is again obtained by enforcing a force-free condition along the x-axis. The results, shown in Figure 4.18, demonstrate that slipping occurs only when the cylinder is both long ($L = 6$) and the axial domain width is relatively small ($W_y = 7$). This behavior contrasts sharply with the 2-D simulations, where similar geometric parameters led to consistent motion. The absence of slipping in shorter cylinders reflects the diminished influence of wall-induced pressure gradients and shear stresses.

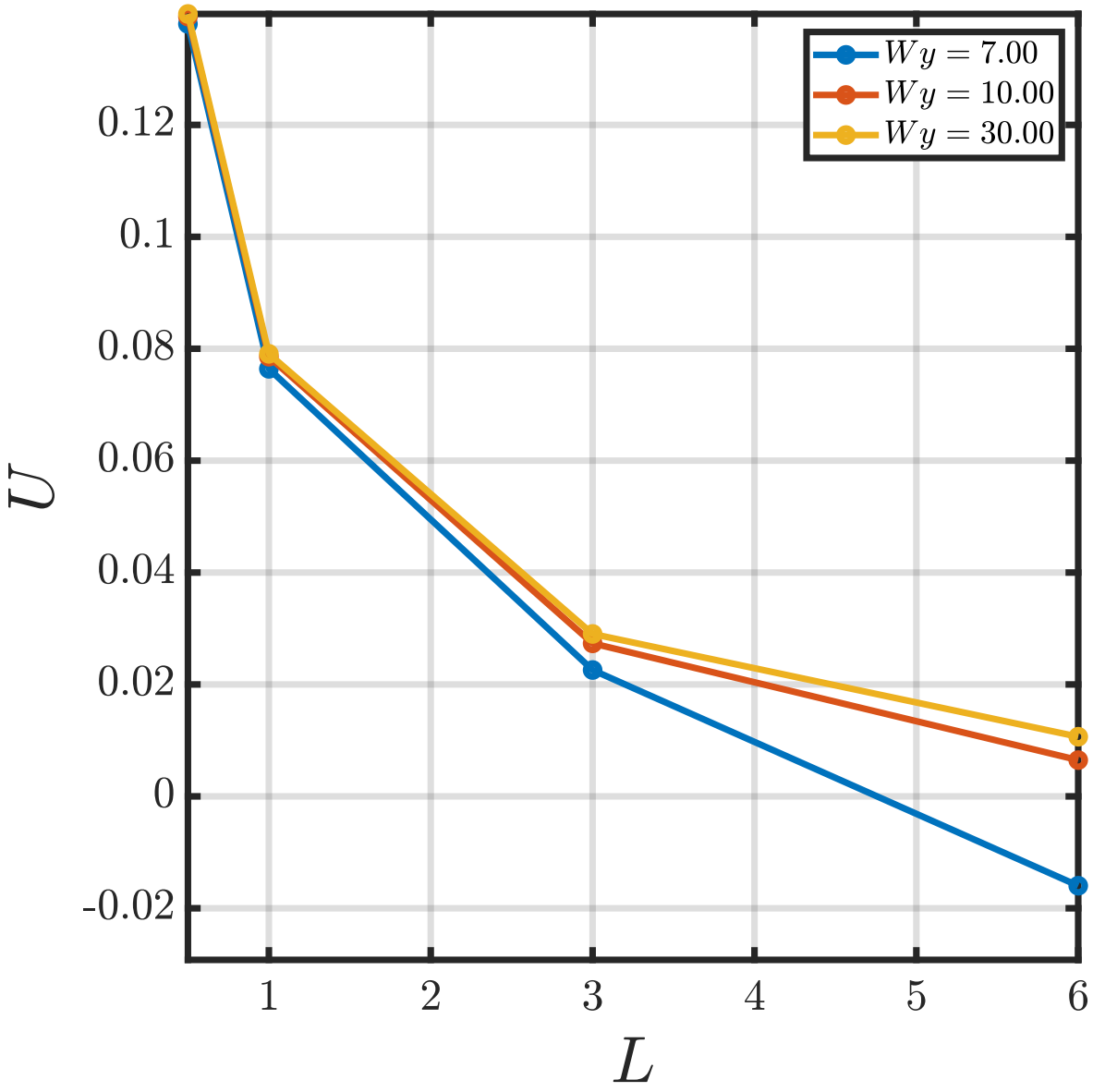

Figure 4.18 Translational velocity of the cylinder under open tank confinement in 3-D for various W_y values. Slipping occurs only for the case $L/D = 6$, $W_y = 7$.

To investigate this behavior in greater detail, the forces and torques acting on the rotating, fixed-position cylinder are decomposed into contributions from the lateral sides and the end caps. In addition, pressure-driven and viscous components are considered separately to clarify their respective roles. As illustrated in Figure 4.19, the total force in the x-direction reverses only for the configuration with $L = 6$ and $W_y = 7$, consistent with the corresponding force-free simulations, where the cylinder exhibits backward slip.

When the total force is partitioned into side and cap contributions, trends similar to those observed in the channel and closed-tank confinements emerge. As in those cases, the relative importance of cap forces diminishes with increasing cylinder length and becomes particularly sensitive when the clearance between the cylinder ends and the back wall is small. By contrast, deviations in the lateral side forces appear once the cylinder reaches moderate lengths (e.g., $L \geq 3$), at which point the overall flow structure begins to shift.

Quantitatively, short cylinders exhibit a relatively stable cap contribution of approximately 28–30% of the total lateral force. For the moderate cylinder length ($L = 3$), the cap contribution in the short-domain case rises to 36%. In contrast, in the long-domain case it decreases to 29%, a value comparable to that of the short-cylinder configuration. For the long cylinder ($L = 6$), this trend is reversed: the cap forces contribute only about 7% of the total force in short domains, while in long domains their contribution increases to 41%. Notably, in contrast to the earlier confinement cases, the long-cylinder configuration with a moderate domain length shows a markedly higher cap contribution of approximately 61% of the total force in the x-direction, underscoring the sensitivity of the force distribution to the combined effects of cylinder length and axial confinement.

To elucidate the underlying hydrodynamic mechanisms, the lateral forces are decomposed into their shear- and pressure-driven components. Both contributions increase with cylinder length, as expected under Stokes flow conditions. However, it is their relative balance, particularly on the cylinder sides, that determines the direction of net motion. In most cases, the net lateral force on the cylinder sides remains positive, indicating that the shear-driven forces, which promote forward translation, dominate. Backward slipping occurs only when the pressure-driven contribution exceeds the opposing shear-driven forces.

This behavior can be better understood by examining the relative growth rates of the two contributions. For shorter domain lengths, the shear-driven force increases by approximately 8.35% with cylinder length, whereas the pressure-driven component grows by 19.7%. In contrast, for longer domains, the pressure-driven forces increase by 18.84%, while the shear-driven forces grow by only 9%. The comparatively stronger growth of the pressure contribution in confined, short-domain configurations is sufficient to reverse the

direction of motion, producing backward slip for long cylinders.

These findings highlight the critical role of axial confinement in establishing the hydrodynamic conditions necessary for slip. In narrow domains, confinement amplifies the pressure gradients around the cylinder, enabling pressure forces to dominate over shear forces. By contrast, in wider domains, the flow is able to bypass the cylinder more effectively, diminishing the influence of pressure gradients and thereby suppressing the slipping mechanism.

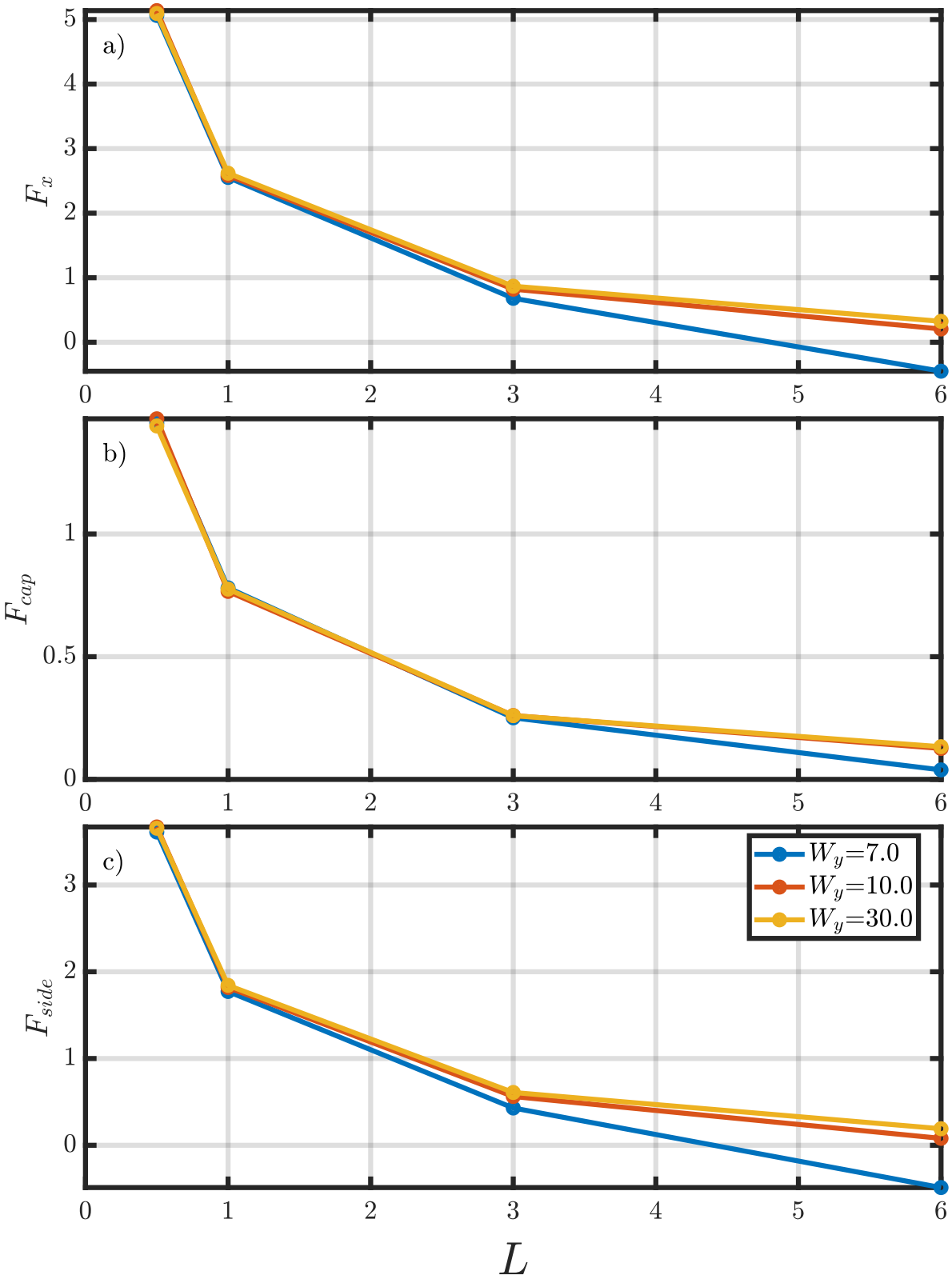

Figure 4.19 Hydrodynamic forces and torques on a finite-length cylinder under open tank confinement with varying W_y. a) Total force in the x-direction; b) Force on end caps; c) Force on sides; Slipping occurs only in the high-aspect-ratio, narrow-domain case.

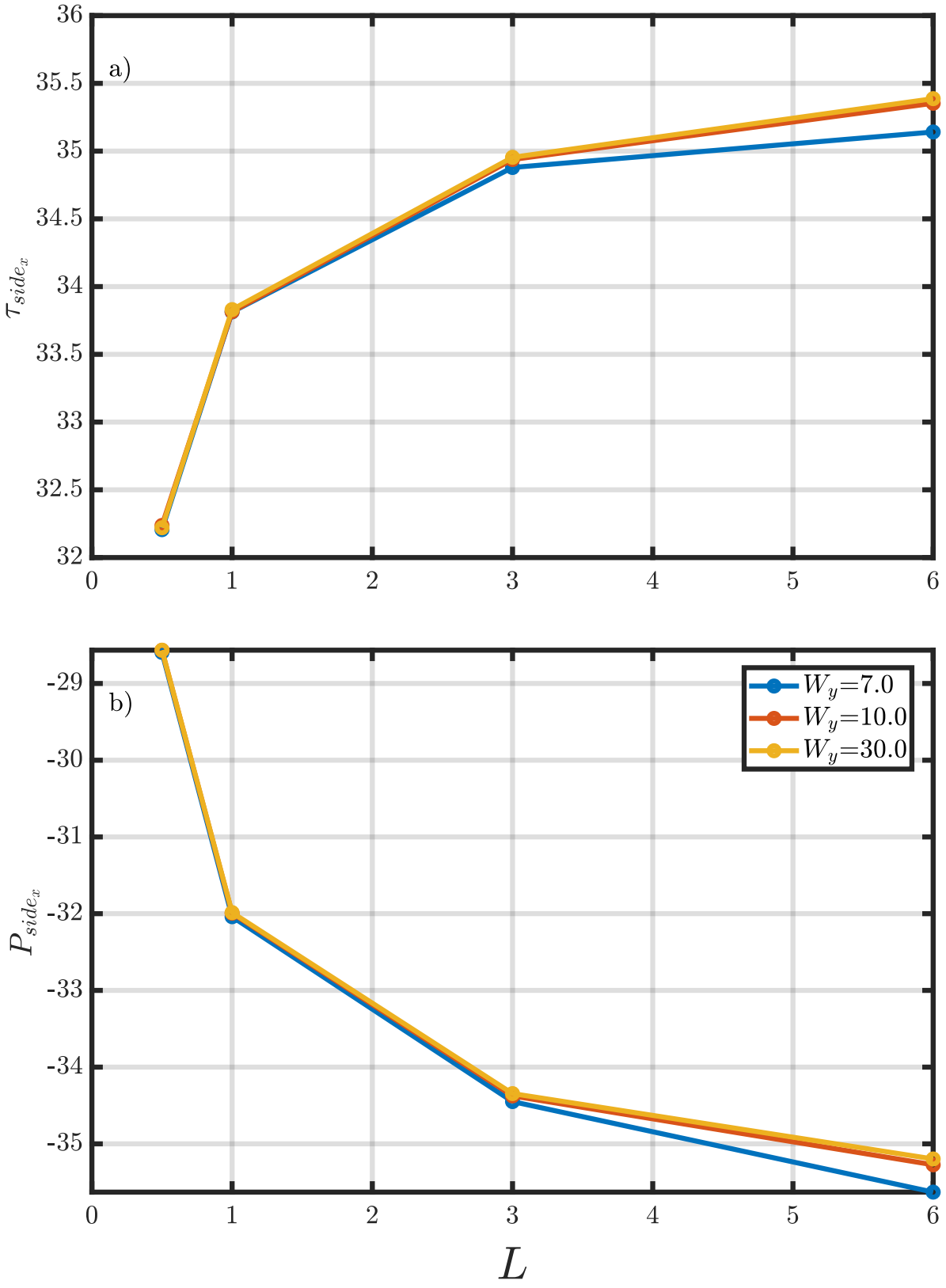

Figure 4.20 Hydrodynamic forces and torques acting on a finite-length cylinder's side with varying W_y under open tank confinement. a) Shear-induced torque on the sides; b) Pressure force on the sides;

5. DISCUSSION & CONCLUSION

5.1 Discussion

For the case of an infinite cylinder, the role of confinement is critical in determining the direction and magnitude of its motion. When comparing different confinement types, it is evident that as the cylinder approaches the wall ($d_{\text{wall}} \to 0$), it behaves as though it is in contact with the boundary. However, as the gap increases, notable differences in the cylinder's behavior emerge. Under fully confined conditions, the cylinder consistently exhibits slipping motion regardless of the bounding box dimensions. Nevertheless, beyond a certain box depth, this slipping velocity saturates, and further increases in domain aspect ratio no longer impact the result. In contrast, under channel and open tank configurations, the direction of motion becomes highly sensitive to the aspect ratio of the domain. In channel confinement, both forward and backward motion are observed, with backward slipping dominating as the box width increases relative to its height. Open tank conditions demonstrate the opposite behavior: slipping occurs in shallow domains but with considerably lower magnitude compared to channel confinement.

These trends are further clarified through the analysis of hydrodynamic forces acting on the cylinder. As expected, the viscous torque remains consistent across all confinement types and aspect ratios, aligning well with the analytical predictions by Jeffrey & Onishi (1981). However, the lateral hydrodynamic force in the x-direction follows a nearly constant trend across small wall distances and only begins to deviate when the cylinder is sufficiently far from the wall for the confinement to influence the global flow field. The deviation between the numerically computed F_x and its analytical counterpart, valid in unbounded domains, captures the effect of confinement on the surrounding flow. This deviation plays a decisive role in determining the net motion of the cylinder, both in

direction and magnitude.

The behavior of finite-length cylinders presents a more complex picture. When the aspect ratio of the bounding box is fixed at 3, the 2-D simulations generally show backward slipping motion under all confinement types, with the exception of the open tank scenario. In 3-D, however, short cylinders remain stationary under all conditions. Slipping only emerges when the cylinder is sufficiently long, and even then, it depends heavily on the confinement type. In channel confinement, long cylinders slip regardless of the box depth W_y. Under closed tank conditions, slipping is observed only when the box is shallow to moderately deep. In the open tank scenario, slipping is confined to configurations where the box is narrow and the cylinder is long. These results highlight the three-dimensional sensitivity of the problem and demonstrate that motion patterns absent in 2-D simulations may appear in 3-D due to additional flow degrees of freedom. For instance, while a 2-D cylinder under open tank confinement and $W_x/W_z = 3$ does not slip, its 3-D counterpart does so when L is high and W_y is small. Similarly, although the closed tank configuration consistently results in slipping in 2-D, in 3-D this only occurs under the right combination of cylinder length and bounding box depth.

To rationalize these results, a detailed force decomposition was performed. The total hydrodynamic force acting on the cylinder was split into side and end contributions as follows:

$$\sum_{\text{cyl}} \mathbf{F} = \sum_{\text{side}} \mathbf{F} + \sum_{\text{cap}} \mathbf{F} \tag{5.1}$$

This decomposition revealed that the length of the cylinder strongly influences the relative contribution of these components. As shown in Figures 4.7, 4.13, and 4.19, increasing the cylinder length L shifts the dominance of the total force from the cylinder's end caps to its side walls.

The side force component, $\sum_{\text{side}} \mathbf{F}$, is primarily governed by lubrication effects in the narrow nip region between the cylinder and the wall, such that:

$$\sum_{\text{side}} \mathbf{F} \approx \sum_{\text{nip}} \mathbf{F}$$

For further clarity, the side force is decomposed into pressure-driven and shear-driven components:

$$\sum_{\text{side}} \mathbf{F} = \sum_{\text{side}} \mathbf{F}^{p} + \sum_{\text{side}} \mathbf{F}^{\text{shear}} \tag{5.2}$$

This distinction is instrumental in understanding the origin of the observed motion. When shear forces dominate, they generate a net positive traction due to the clockwise rotation of the cylinder, which results in forward motion. Conversely, when pressure forces exceed shear contributions, the resulting negative net force drives backward slipping. It is important to note that because the cylinder's rotation direction is fixed, shear-induced forces consistently promote forward motion, making pressure forces the critical factor in determining whether slipping occurs.

Finally, the end cap forces $\sum_{\text{cap}} \mathbf{F}$ are where three-dimensional effects become prominent, as they capture the flow-induced forces and drag arising from the interaction with the external flow field. These forces are velocity-dependent and can be expressed as:

$$\sum_{\text{cap}} \mathbf{F} = \left| \sum_{\text{cap}} \mathbf{F}^{\text{flow}} \right| - \left| \sum_{\text{cap}} \mathbf{F}^{\text{drag}} \right| \quad \text{for } U > 0 \tag{5.3}$$

$$\sum_{\text{cap}} \mathbf{F} = \left| \sum_{\text{cap}} \mathbf{F}^{\text{flow}} \right| + \left| \sum_{\text{cap}} \mathbf{F}^{\text{drag}} \right| \quad \text{for } U < 0 \tag{5.4}$$

These expressions show that when the cylinder moves forward, the drag opposes the flow-induced pressure forces, reducing the net cap contribution. In contrast, during backward motion, both effects add constructively, further reinforcing the motion. This further supports the finding that the relative magnitude and direction of side and cap forces, governed by confinement geometry and cylinder length, serve as the primary determinants of translational behavior.

This study investigated the motion of both infinite and finite-length cylinders rotating near a wall under different confinement conditions. The results demonstrate that confinement geometry and domain aspect ratio are crucial in determining not only the magnitude but also the direction of translational motion. While infinite cylinders show consistent behavior across configurations, finite-length cylinders exhibit more complex dynamics, with slipping behavior emerging only under specific conditions of cylinder length and

bounding box dimensions.

The accompanying force analysis revealed that the net direction of motion is determined by the balance between shear and pressure forces acting on the cylinder's sides. Shear forces arising from viscous traction consistently promote forward motion, whereas pressure forces—amplified by geometric confinement—can induce backward slipping. Additionally, flow-induced and drag-related forces on the end caps gain prominence in finite cylinders, contributing further to the overall dynamics. These findings underscore the limitations of purely two-dimensional analyses and emphasize the importance of three-dimensional modeling when predicting real-world behavior of cylindrical bodies in confined viscous flows.

5.2 Conclusion

This study demonstrates that the cylinder's motion near a planar wall is jointly controlled by gap height, domain aspect ratio, and the specific confinement geometry. For the 2D (effectively infinite-length) problem, increasing the wall–cylinder gap reduces wall-induced drag and increases speed, while confinement keeps the force balance distinct from the unbounded case. Crucially, aspect ratio does not act alone: in channel-type confinement, slip appears once the aspect ratio exceeds roughly two, whereas in open-tank confinement, the trend reverses and slip is promoted below that threshold. In closed-tank confinement, slip persists across aspect ratios but its magnitude saturates once the aspect ratio is about three. The 2D results also highlight the role of the top boundary, with force components remaining at an order-one magnitude in both the streamwise and wall-normal directions across the parameter range.

The fully 3D (finite-length) simulations demonstrate that 2D predictions are not generally representative because torque–force coupling and end effects can flip the direction of motion. Cases that translate forward in 2D may slip in 3D (e.g., open-tank with long cylinders in short domains), while the opposite can occur for longer domains in channel and closed-tank configurations. The main contributions of this work are: a unified comparison across channel, open-tank, and closed-tank confinements that identifies the reversal of aspect-ratio thresholds and the saturation of slip; a clear demonstration of how 3D end effects reweight cap versus side contributions and thereby overturn 2D

trends; and a qualitative force-decomposition framework that diagnoses when pressure-driven side forces dominate shear-driven contributions, providing a practical criterion to anticipate slip versus forward translation. Together, these results explain when and why confinement induces or suppresses slip, clarify the limits of 2D surrogates, and offer a usable guide for predicting motion in constrained microfluidic and robotic settings.

5.3 Future Work

A key next step is an experimental program that validates and extends these findings by rotating a magnetized cylinder near a wall with electromagnetic actuation. Initial trials with Helmholtz coils showed that, due to the high sensitivity of the magnetic field to coil alignment and current imbalance, the observed *translation* of the cylinder can be dominated by unintended electromagnetic forces (from small field gradients), making it difficult to isolate hydrodynamic slip. To address this, we propose a closed-loop, vision-based control experiment that deliberately *nulls* translation while the cylinder is rotated at a prescribed rate, and then uses the control effort as a readout of the hydrodynamic tendency.

Concretely, a uniform, rotating field $\mathbf{B}(t)$ (Helmholtz pair) sets the spin rate Ω about $+y$, while an independent gradient channel (e.g., a Maxwell/anti-Helmholtz pair along x) applies a small, controllable magnetic force F_x^{EM} via calibrated coil currents. A real-time vision loop (frame-rate $\gtrsim$100 Hz) holds the cylinder's x-position fixed ($U \approx 0$) by adjusting the gradient current to cancel any hydrodynamic drift. In steady state,

$$F_x^{\mathrm{EM}} + F_x^{\mathrm{hyd}}(d_{\mathrm{wall}}, L, W_y, \Omega) \;=\; 0 \quad\Longrightarrow\quad F_x^{\mathrm{hyd}} \;=\; -\,F_x^{\mathrm{EM}} \tag{5.5}$$

so the sign and magnitude of the required coil current directly report the direction and strength of the slip that would occur under force-free conditions. With a one-time calibration of the actuation map

$$\begin{bmatrix} \mathbf{B} \\ \nabla\mathbf{B} \end{bmatrix} = \mathbf{A}\,\mathbf{i}, \qquad F_x^{\mathrm{EM}} \approx \mathbf{c}_x^{\top}\mathbf{i} \tag{5.6}$$

(where $\mathbf{i}$ are coil currents and $\mathbf{c}_x$ is obtained from measurements with the cylinder far from boundaries), the experiment can quantitatively recover F_x^{hyd} versus the gap ratio d_{wall}, the cylinder length L, and axial confinement W_y.

Practically, the setup would use a high-viscosity working fluid (e.g., silicone oils) and frequencies ensuring $Re \ll 1$, a rigid cylinder with a magnetic moment aligned to $+y$ (e.g. Neodymium Magnets that are magnetized across the diameter), and a glass/PDMS chip that realizes the three confinements studied numerically (channel, closed tank, open tank). Micro-PIV can capture surrounding flow to corroborate shear/pressure trends; the rolling check $U \to \Omega R$ as $d_{\mathrm{wall}} \to 0$ and the Jeffrey & Onishi torque curve provide internal benchmarks. Control-wise, an inner loop regulates Ω via the rotating uniform field while an outer loop regulates x-position via the gradient; the logged gradient currents (after baseline subtraction measured far from walls) yield F_x^{hyd} and its sign.

This approach enables four targeted validations: (i) reproduce forward/backward direction reversals as functions of d_{wall} and domain aspect ratios; (ii) demonstrate saturation of backward slip in closed tanks at large W_x/W_z; (iii) show that 3-D slip emerges only beyond a critical L and is strongly modulated by W_y; and (iv) separate "cap-dominated" from "side-dominated" regimes by varying L at fixed d_{wall} and W_y. Extensions include deformable (soft) walls to probe elastohydrodynamic amplification of pressure loads, weak-inertia tests ($Re \sim 10^{-1}$) to assess robustness of direction maps, and noncircular cross-sections to quantify shape sensitivity. Finally, compiling phase diagrams for $\mathrm{sign}(U)$ and $|U|$ over $(d_{\mathrm{wall}}, W_x/W_z)$ in 2-D and $(d_{\mathrm{wall}}, L, W_y)$ in 3-D—together with simple pumping metrics (flux per unit torque) in channel mode—would translate the fundamental mechanisms into actionable design guidance.

BIBLIOGRAPHY

Abel, J. S., Stangle, G. C., Schilling, C. H., & Aksay, I. A. (1994). Sedimentation in flocculating colloidal suspensions. *Journal of Materials Research*, *9*(2), 451–461.

Acemoglu, A. & Yesilyurt, S. (2015). Effects of poiseuille flows on swimming of magnetic helical robots in circular channels. *Microfluidics and Nanofluidics*, *19*(5), 1109–1122.

Batchelor, G. K. (1970). Slender-body theory for particles of arbitrary cross-section in Stokes flow. *Journal of Fluid Mechanics*, *44*(3), 419–440.

Caldag, H. O., Acemoglu, A., & Yesilyurt, S. (2017). Experimental characterization of helical swimming trajectories in circular channels. *Microfluidics and Nanofluidics*, *21*(8), 136.

Caldag, H. O., Demir, E., & Yesilyurt, S. (2022). A numerical and experimental investigation of rolling and sliding motion of rotating spheres inside a cylinder. *Journal of Fluid Mechanics*, *935*, A9.

Caldag, H. O. & Yesilyurt, S. (2019). Trajectories of magnetically-actuated helical swimmers in cylindrical channels at low Reynolds numbers. *Journal of Fluids and Structures*, *90*, 164–176.

Choi, H.-I., Lee, Y., Choi, D.-H., & Maeng, J.-S. (2010). Design optimization of a viscous micropump with two rotating cylinders for maximizing efficiency. *Structural and Multidisciplinary Optimization*, *40*(1), 537–548.

Cox, R. G. (1970). The motion of long slender bodies in a viscous fluid Part 1. General theory. *Journal of Fluid Mechanics*, *44*(4), 791–810.

Crowdy, D. (2011). Treadmilling swimmers near a no-slip wall at low Reynolds number. *International Journal of Non-Linear Mechanics*, *46*(4), 577–585.

Czajka, P., Antosiewicz, J. M., & Długosz, M. (2019). Effects of Hydrodynamic Interactions on the Near-Surface Diffusion of Spheroidal Molecules. *ACS Omega*, *4*(16), 17016–17030. Publisher: American Chemical Society.

Daddi-Moussa-Ider, A., Nasouri, B., Vilfan, A., & Golestanian, R. (2021). Optimal swimmers can be pullers, pushers or neutral depending on the shape. *Journal of Fluid Mechanics*, *922*, R5.

Das, D. & Lauga, E. (2018). Computing the motor torque of Escherichia coli. *Soft Matter*, *14*(29), 5955–5967. Publisher: The Royal Society of Chemistry.

Davis, A. M. J. (1993). Stokes drag on a disk sedimenting edgewise toward a plane wall. *Journal of Engineering Mathematics*, *27*(2), 209–219.

Day, R. F. & Stone, H. A. (2000). Lubrication analysis and boundary integral simulations

of a viscous micropump. *Journal of Fluid Mechanics*, *416*, 197–216.

De Mestre, N. J. & Russel, W. B. (1975). Low-Reynolds-number translation of a slender cylinder near a plane wall. *Journal of Engineering Mathematics*, *9*(2), 81–91.

Dong, X., Lum, G. Z., Hu, W., Zhang, R., Ren, Z., Onck, P. R., & Sitti, M. (2020). Bioinspired cilia arrays with programmable nonreciprocal motion and metachronal coordination. *Science Advances*, *6*(45), eabc9323. Publisher: American Association for the Advancement of Science.

Gavze, E. & Shapiro, M. (1997). Particles in a shear flow near a solid wall: Effect of nonsphericity on forces and velocities. *International Journal of Multiphase Flow*, *23*(1), 155–182.

Goldman, A. J., Cox, R. G., & Brenner, H. (1967). Slow viscous motion of a sphere parallel to a plane wall—I Motion through a quiescent fluid. *Chemical Engineering Science*, *22*(4), 637–651.

Happel, J. & Brenner, H. (1983). *Low Reynolds number hydrodynamics: with special applications to particulate media*, volume 1 of *Mechanics of fluids and transport processes*. Dordrecht: Springer Netherlands.

Hinch, E. J. (1972). Note on the symmetries of certain material tensors for a particle in Stokes flow. *Journal of Fluid Mechanics*, *54*(3), 423–425.

Ishimoto, K. & Gaffney, E. A. (2013). Squirmer dynamics near a boundary. *Physical Review E*, *88*(6), 062702. Publisher: American Physical Society.

Jeffery, G. B. & Filon, L. N. G. (1922). The rotation of two circular cylinders in a viscous fluid. *Proceedings of the Royal Society of London. Series A, Containing Papers of a Mathematical and Physical Character*, *101*(709), 169–174. _eprint: https://royalsocietypublishing.org/doi/pdf/10.1098/rspa.1922.0035.

Jeffrey, D. J. & Onishi, Y. (1981). The Slow Motion of a Cylinder Next to a Plane Wall. *The Quarterly Journal of Mechanics and Applied Mathematics*, *34*(2), 129–137. _eprint: https://academic.oup.com/qjmam/article-pdf/34/2/129/5169643/34-2-129.pdf.

Katz, D. F., Blake, J. R., & Paveri-Fontana, S. L. (1975). On the movement of slender bodies near plane boundaries at low Reynolds number. *Journal of Fluid Mechanics*, *72*(3), 529–540.

Koens, L. & Montenegro-Johnson, T. D. (2021). Local drag of a slender rod parallel to a plane wall in a viscous fluid. *Physical Review Fluids*, *6*(6), 064101. Publisher: American Physical Society.

Lauga, E., DiLuzio, W. R., Whitesides, G. M., & Stone, H. A. (2006). Swimming in Circles: Motion of Bacteria near Solid Boundaries. *Biophysical Journal*, *90*(2), 400–412.

Leal, L. G. (2007). *Advanced Transport Phenomena: Fluid Mechanics and Convective*

Transport Processes. Cambridge Series in Chemical Engineering. Cambridge: Cambridge University Press.

Merlen, A. & Frankiewicz, C. (2011). Cylinder rolling on a wall at low Reynolds numbers. *Journal of Fluid Mechanics*, *685*, 461–494.

Mestre, N. J. d. (1973). Low-Reynolds-number fall of slender cylinders near boundaries. *Journal of Fluid Mechanics*, *58*(4), 641–656.

Mitchell, W. H. & Spagnolie, S. E. (2015). Sedimentation of spheroidal bodies near walls in viscous fluids: glancing, reversing, tumbling and sliding. *Journal of Fluid Mechanics*, *772*, 600–629.

O'Neill, M. E. (1964). A Slow motion of viscous liquid caused by a slowly moving solid sphere. *Mathematika*, *11*(1), 67–74. _eprint: https://londmathsoc.onlinelibrary.wiley.com/doi/pdf/10.1112/S0025579300003508.

Pak, O. S. & Lauga, E. (2014). Theoretical models in low-Reynolds-number locomotion. arXiv:1410.4321 [physics].

Rallabandi, B., Saintyves, B., Jules, T., Salez, T., Schönecker, C., Mahadevan, L., & Stone, H. A. (2017). Rotation of an immersed cylinder sliding near a thin elastic coating. *Physical Review Fluids*, *2*(7), 074102. Publisher: American Physical Society.

Ray, M. (1936). XLVI. Application of Bessel functions to the solution of problem of motion of a circular disk in viscous liquid. *The London, Edinburgh, and Dublin Philosophical Magazine and Journal of Science*, *21*(141), 546–564. Publisher: Taylor & Francis _eprint: https://doi.org/10.1080/14786443608561607.

Saintyves, B., Rallabandi, B., Jules, T., Ault, J., Salez, T., Schönecker, C., Stone, H. A., & Mahadevan, L. (2020). Rotation of a submerged finite cylinder moving down a soft incline. *Soft Matter*, *16*(16), 4000–4007. Publisher: The Royal Society of Chemistry.

Salez, T. & Mahadevan, L. (2015). Elastohydrodynamics of a sliding, spinning and sedimenting cylinder near a soft wall. *Journal of Fluid Mechanics*, *779*, 181–196.

Seddon, J. R. T. & Mullin, T. (2006). Reverse rotation of a cylinder near a wall. *Physics of Fluids*, *18*(4), 041703.

Sen, M., Wajerski, D., & Gad-el Hak, M. (1996). A Novel Pump for MEMS Applications. *Journal of Fluids Engineering*, *118*(3), 624–627.

Spagnolie, S. E. & Lauga, E. (2012). Hydrodynamics of self-propulsion near a boundary: predictions and accuracy of far-field approximations. *Journal of Fluid Mechanics*, *700*, 105–147.

Stokes, G. G. (2009). *Analytical Investigation*, (pp. 11–75). Cambridge Library Collection - Mathematics. Cambridge University Press.

Teng, J., Rallabandi, B., Stone, H. A., & Ault, J. T. (2022). Coupling of translation and rotation in the motion of finite-length rods near solid boundaries. *Journal of Fluid Mechanics*, *938*, A30.

Witelski, T. P. (1998). Dynamics of air bearing sliders. *Physics of Fluids*, *10*(3), 698–708.

Zhu, L., Lauga, E., & Brandt, L. (2013). Low-Reynolds-number swimming in a capillary tube. *Journal of Fluid Mechanics*, *726*, 285–311.

Zöttl, A. & Stark, H. (2012). Nonlinear Dynamics of a Microswimmer in Poiseuille Flow. *Physical Review Letters*, *108*(21), 218104. Publisher: American Physical Society.